Computational Aeroacoustic Prediction of Airfoil Self-Noise at Static Angles of Attack

by

Alison Zilstra

A thesis
presented to the University of Waterloo
in fulfillment of the
thesis requirement for the degree of
Master of Applied Science
in
Mechanical Engineering

Waterloo, Ontario, Canada, 2019

I hereby declare that I am the sole author of this thesis. This is a true copy of the thesis, including any required final revisions, as accepted by my examiners.

I understand that my thesis may be made electronically available to the public.

Abstract

Aeroacoustic noise from wind turbines is often an obstacle in the implementation of wind farms. Reduction of this noise is key to allowing the expansion of the wind energy sector which is crucial for decreasing the dependence on fossil fuel energy sources. The use of a fully analytical computational model for aeroacoustic noise will allow for acoustics to be incorporated into the design stage of new wind turbine technologies. This thesis investigates the use of a predictive model for the noise from two dimensional (2D) blade segments using computational fluid dynamics (CFD). The simulation uses Reynolds Averaged Navier-Stokes (RANS) to initialize the simulation, and then a combination of Large Eddy Simulation (LES) and the Ffowcs-Williams and Hawkings (FW-H) acoustic analogy to predict the flow and acoustics, respectively.

The SD 7037 and NACA 0012 airfoils were simulated and compared against experimental flow and acoustics data. The SD 7037 airfoil was tested using incompressible and compressible LES simulation for a Reynolds number of $Re = 4.25 \times 10^4$. The results show good prediction of both the flow and acoustics, and the source of the tonal noise generated by the airfoil at 0° angle of attack (AOA) was determined to be a result of 2D boundary layer behaviour, and also the transition from 2D to 3D behaviour. The 1° AOA results did not predict the tonal noise found in experiments, but it was determined that inaccuracies in some of the simulations caused the boundary layer behaviour to falsely change to that of the experimental 2° or 3° AOA. The NACA 0012 airfoil was tested using incompressible LES for a high Re case of $Re = 1.5 \times 10^6$. The flow simulation for this case was good, however the acoustic prediction was at a higher sound pressure level (SPL) than the experimental data. The second case of this simulation predicted tonal noise when experiments predicted broadband noise only. The simulation of this false tonal noise was attributed to instabilities in the simulation.

The differences between the SD 7037 1° results, where instabilities caused no tones to be simulated, and the NACA 0012 results for the second case, where instabilities caused false tones to be predicted, shows that care must be taken in the setup of the simulation. Recommendations for future work are to perform a grid independence study and sensitivity analysis to determine the cause of these false predictions. That being said, overall, the predictive abilities of the computational aeroacoustic model result in good prediction of the airfoil self-noise for static AOAs.

Acknowledgements

I would like to thank everyone who has supported me while completing my thesis. The guidance and wisdom provided by my supervisor, Professor David A. Johnson, helped me to choose a topic I am truly passionate about and keep my mind on realistic goals. The support of my colleagues Nicholas Tam, Michael McKinnon, Faegheh Ghorbanishohrat and Farid Samara, which made working in windowless offices much less depressing. I also appreciate the support from the faculty and staff in the MME department, with whom I have become quite familiar over the past 7 years.

I am grateful for the opportunities that the University of Waterloo has given to me through my undergraduate and graduate degrees. The ability to try out teaching through TA positions has solidified my decision to one day become a professor, which is something I never thought I would have the courage or knowledge to do. I would also like to thank the funding support provided by the Ontario Graduate Scholarship (OGS) and the facilities of the Shared Hierarchical Academic Research computing Network (SHARCNET) and Compute/Calcul Canada, which all helped to smooth the way to completing my research.

Of course, I could not be where I am today without the unconditional love and support of my family. They always believed in my ability to succeed and never expressed any doubt or negativity towards my goals. They also completely understood when I spent essentially half a year locked away in my office diligently working on my thesis.

And finally I must acknowledge the happiness brought to my life by my two cats, Penny and Sheldon, whom I adopted when I began my graduate program.

Table of Contents

List of Tables

List of Figures

Abbreviations

AOA Angle of Attack.

CAA Computational Aeroacoustics.

CFD Computational Fluid Dynamics.

CFL Courant Number.

FFT Fast Fourier Transform.

FW-H Ffowcs-Williams and Hawkings.

HAWT Horizontal Axis Wind Turbine.

LBL-VS Laminar Boundary Layer - Vortex Shedding.

LE Leading Edge.

LES Large Eddy Simulation.

LSB Laminar Separation Bubble.

MFRT Mean Flow Residence Time.

MW Megawatt.

NREL National Renewable Energy Laboratory.

PIV Particle Image Velocimetry.

RANS Reynolds-Averaged Navier-Stokes.

RMS Root-Mean-Square.

SIMPLEC Semi-Implicit Method for Pressure-Linked Equations - Consistent.

SPL Sound Pressure Level.

TBL-TE Turbulent Boundary Layer - Trailing Edge.

TE Trailing Edge.

UDF User-Defined Functions.

List of Symbols

Roman Symbols

a	Axial induction factor.
a'	Angular induction factor.
C_d	Drag coefficient.
C_f	Skin friction coefficient.
C_l	Lift coefficient.
C_p	Pressure coefficient.
D	Drag force $[N]$.
f	Frequency $[Hz]$.
F_N	The force perpindicular to the blade rotation plane $[N]$.
F_T	The force in the blade rotation plane that generates torque to cause rotor motion $[N]$.
H	Boundary layer shape factor.
L	Lift force $[N]$.
L_p	Sound pressure level (SPL) $[dB]$.
p	Pressure, and acoustic pressure $[Pa]$.
$\hat{p}$	Root mean square sound pressure $[Pa]$.

r	Radial distance of blade segment from rotor centre $[m]$.
Re	Reynolds number.
T_{ij}	Lighthill's tensor.
t	Time $[s]$.
U_∞	Free stream velocity, either incoming wind velocity or wind tunnel velocity $[m/s]$.
W	Relative wind velocity for a wind turbine blade at a given location $[m/s]$.

Greek Letters

α	Angle of attack (AOA) for an airfoil $[^\circ]$.
β	Chord line angle $[^\circ]$.
λ	Acoustic wavelength $[m]$.
Ω	Rotational speed of rotor [rad/s].
ϕ	Relative wind speed angle $[^\circ]$.
τ_w	Wall shear stress $[Pa]$.
τ	Time in the retarded time frame $[s]$.

Chapter 1

Introduction

Wind turbines are a prominent renewable energy technology, and wind farm developers often face difficulties with acceptance due to the aeroacoustic noise they generate. The interaction between the wind and the blades causes the energy extraction, and is also the source of this noise. The development of quieter blades and other noise reduction technologies requires a deep understanding of the aeroacoustic behaviour of the blades as they rotate. Unfortunately, the scale of modern wind turbines do not allow them to be accurately scaled for controlled wind tunnel testing, and full scale testing is expensive and uncontrolled. This means the design of quieter wind turbines is heavily dependant on predictive models to allow acoustic analysis during the design stage of a wind turbine. Semi-empirical models are available for cases where experimental data already exists, but for new technologies, fully analytical models are required to predict the noise. With the increasing computational power of Computational Fluid Dynamics (CFD) software, it is possible to perform complex acoustic simulations of wind turbines to determine the aeroacoustic noise emitted by the specific design. Building confidence in these models requires validation of simpler, controlled cases before applying the prediction model to a full wind turbine. This research investigates the computational aeroacoustic prediction of airfoil self-noise at static Angle of Attack (AOA)s. The simulations were conducted using the CFD software ANSYS Fluent, and use Large Eddy Simulation (LES) and the Ffowcs-Williams and Hawkings (FW-H) acoustic model to generate the prediction. The results from these simulations are validated through comparison with flow and acoustic data from existing experiments.

1.1 Motivation

This research is motivated by the need to make renewable energy sources more appealing to the general public. The issue of aeroacoustic noise emitted by wind turbines is a factor in preventing the full use of this technology, and therefore any advancements in the design of quieter wind turbines would be beneficial. Experimental methods for determining the noise emitted from new wind turbine designs either require full scale testing, which is costly, or smaller scale testing, which fails to incorporate all the complexities. The ability to use computational aeroacoustic simulations in the design stages of a new turbine, or a new noise reduction technology, would facilitate the design of quieter turbine blades.

1.2 Objective

The objective of this research is to determine the feasibility of using computational aeroacoustic simulations to predict the airfoil self-noise generated at static angles of attack. This is tested through simulations of an airfoil designed for use on wind turbines, SD-7037, as well as the NACA 0012 airfoil since it is often used in research and has well understood behaviour. The simulated acoustic spectra are validated through comparison with experimental data for the same Reynolds number.

1.3 Thesis Organization

This thesis is structured as follows:

Chapter 2 provides background information required for the full understanding of the analysis and results. The aerodynamic behaviour of wind turbines and airfoils is explained, as well as the acoustic theory behind airfoil self-noise and wind turbine noise. The current status of aeroacoustic prediction models is given, along with the general derivation of the FW-H model that is used for this research. Finally, the relevant experimental and computational research is summarized.

Chapter 3 covers the CFD and Computational Aeroacoustics (CAA) models used for this research, which are all existing models in the ANSYS Fluent software.

Chapter 4 summarizes the numerical setup for the NACA 0012 and SD 7037 cases, including the geometry, mesh, boundary conditions and solver setup. The method used to post-process the acoustic receiver data in Matlab is also included.

Chapter 5 discusses the results for the SD 7037 cases, and draws conclusions about the predictive ability of the flow and acoustic simulations. There is also discussion about the flow patterns that cause the tonal noise components found in the experimental recordings.

Chapter 6 discusses the results for the NACA 0012 cases and compares them to the results from the SD 7037 cases. Suggestions are also made for future studies to improve the accuracy of the simulated results.

Chapter 7 covers the conclusions of this thesis and the recommendations for future work.

Chapter 2

Background

This chapter covers the background information on the main concepts required for this research. Aeroacoustic prediction for wind turbines draws on theory from two main areas: fluid dynamics and acoustics. These concepts are combined together to create the semi-empirical and analytical models used to predict the aeroacoustic noise created by a wind turbine. Though the simulations conducted in this research are for 2D predictions, an understanding of the 3D behaviour of wind turbines is necessary when considering the ability of this model to succeed in full wind turbine acoustic prediction.

2.1 Horizontal Axis Wind Turbines

The type of wind turbine considered in this research is a standard horizontal axis wind turbine, with a three blade rotor that is mounted upwind of the tower. The major elements of a wind turbine can be seen in Figure 2.1. The fluid dynamics essentials of a wind turbine are the relative velocity triangle formed by the corrected incoming wind velocity, $U_\infty(1-a)$, and the corrected rotational velocity of the blade, $\Omega r(1+a')$. The relative velocity, W, is used to determine the effective AOA, α, and the lift and drag force vector, as seen in Figure 2.2. The combination of the lift, L, and drag, D, vectors in the direction of rotation gives the torque, F_T, generated by the turbine. The torque is calculated for a section of the blade of length Δr, as shown in Equation (2.1) and (2.2).

$$F_t = L\sin\phi - D\cos\phi \tag{2.1}$$

where,

$$L = \frac{1}{2}\rho W^2 C_l c \Delta r$$
$$D = \frac{1}{2}\rho W^2 C_d c \Delta r \tag{2.2}$$

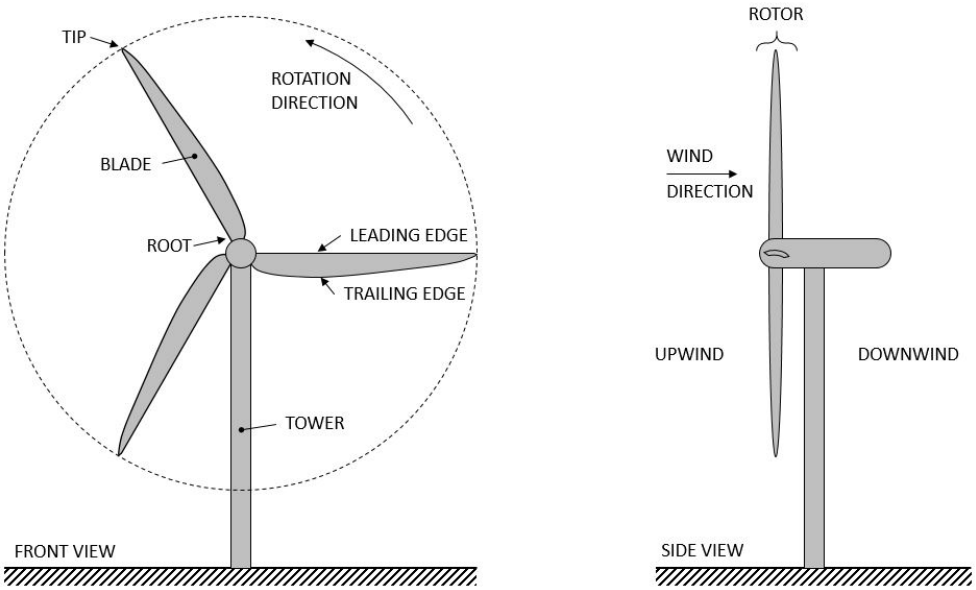

Figure 2.1: Horizontal Axis Wind Turbine (HAWT) diagram

The outer portion of the blade has a larger relative wind velocity due to the larger rotational velocity component. This area is of high importance for the efficiency of wind turbines since the higher relative wind speed and larger radius results in a higher torque and therefore more power generation. When studying this area of interest, it is possible to create a simplified representation of the complex blade geometry and motion with a 2D blade segment in a wind tunnel. This requires using the blade's relative velocity, W, as the wind tunnel velocity and effective AOA, α, as the AOA for the blade segment. This is an approximation since it is neglecting many complexities such as any twist or changes in chord length in the blade, but it allows for controlled testing of new designs or design modifications. This simplification can also be used for CFD simulations of wind turbine blades.

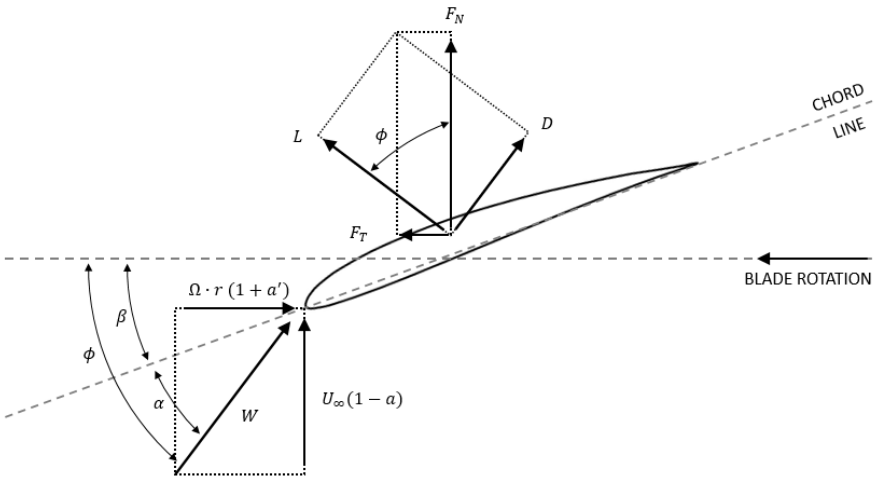

Figure 2.2: Relative velocity triangle and resulting forces for a wind turbine blade

2.1.1 Airfoil Boundary Layer Theory

An important factor in the design of wind turbines is the lift and drag properties of the blade, which is highly dependent on many factors including the boundary layer behaviour over the blade. When a boundary layer develops on a surface, it begins as a laminar boundary layer and then transitions to a turbulent boundary layer. This behaviour is shown in Figure 2.3 for a flat plate, which approximates the behaviour over the curved surface of an airfoil. In this figure, location 1 is the laminar region and locations 2 to 5 indicate the long transition region before reaching location 6 of a fully turbulent flow [1]. This transition region emphasizes the change in overall flow behaviour by showing the transition from 2D Tollmein-Schlichting (T-S) waves early in the region to complex 3D vortical structures as the flow approaches complete turbulence [1].

In low Reynolds number flows, this transition occurs over a separated flow region known as a Laminar Separation Bubble (LSB), and the transition to turbulence is what causes the separated laminar flow to reattach to the surface of the airfoil [2]. Boundary layer behaviour can be identified by looking at the shear stress on the surface of the airfoil, since this is dependent on the velocity behaviour at the surface. This includes experimental methods such as surface oil flow visualization, but can also be examined through simulations with contours or plots of the shear stress, τ_w in Equation 2.3, and its corresponding skin friction coefficient, C_f in Equation 2.4. This is especially useful for identifying the location of the LSB since the separated region has shear stress values that approach zero due to the

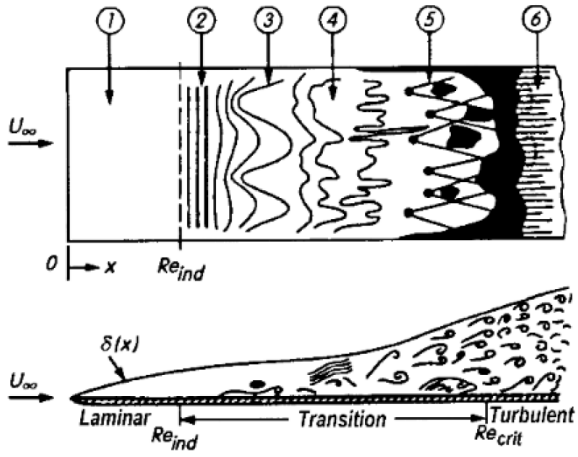

Figure 2.3: Boundary layer transition for a flat plate [1]

stagnant air trapped within. Another boundary layer behaviour indicator is the shape factor, H, which reaches a maximum value when the wake transitions to turbulence [2]. Shape factor is the ratio between the displacement thickness and momentum thickness of a boundary layer, where displacement thickness is the height added to the boundary layer due to the velocity deficit at the surface and momentum thickness is the loss of momentum due to the velocity deficit [3]. These methods are useful for defining the behaviour in the boundary layer and on the surface of the airfoil, since this has a large impact on the acoustic behaviour, as will be explained in Section 2.3.1.

$$\tau_w = \mu \frac{dU}{dy} \tag{2.3}$$

$$C_f = \frac{\tau_w}{\frac{1}{2}\rho U^2} \tag{2.4}$$

2.2 Acoustics

A basic understanding of acoustics assists in understanding the mechanisms of wind turbine noise and the interpretation of simulated results. In general, sound consists of small pressure fluctuations that are propagated through a medium at the speed of sound, which is $340m/s$ in air (at standard temperature and pressure). The human ear is only capable

of perceiving sound waves of a certain frequency, f, and amplitude, or pitch and volume, respectively. The audible frequency range, measured in Hertz (Hz), is typically from $20Hz$ to $20kHz$ [4]. The lowest audible sound is at a root mean square of pressure amplitude, $\hat{p}$, equal to $2 \times 10^{-5}Pa$ which serves as the reference for the decibel (dB) scale, and the threshold for pain is set at $\hat{p} = 200Pa$, or $140dB$ [5]. The decibel values given refer to the Sound Pressure Level (SPL), L_p, which is given by Equation 2.5 [5].

$$L_p = 10 \log \left(\frac{\hat{p}^2}{\hat{p}^2_{ref}} \right) \tag{2.5}$$

The sound emitted from a wind turbine blade contains a combination of many frequencies at different SPLs. Analyzing the sound requires breaking down the complex acoustic pressure signal into its individual frequency components, which is accomplished using the Fast Fourier Transform (FFT). The FFT filters the frequency using a consistent bandwidth, Δf, and returns the acoustic pressure amplitude for each band. Once these results are converted to SPL for each band, they are commonly displayed in three ways: narrowband spectra, $\frac{1}{1}$-octave spectra or $\frac{1}{3}$-octave spectra. The narrowband spectra has a consistent bandwidth for the range of frequencies shown, whereas $\frac{1}{1}$-octave and $\frac{1}{3}$-octave condense the data over frequency ranges that increase in size with increasing frequency. For $\frac{1}{1}$-octave bands, the upper bounding frequency is double the lower bounding frequency, and for $\frac{1}{3}$-octave bands, the upper bound is $\sqrt[3]{2}$ times the lower [5]. The simulation results for this research are shown using narrowband to highlight any tonal noise present and $\frac{1}{3}$-octave band spectra to compare the overall patterns in the broadband noise.

2.3 Wind Turbine Aeroacoustics

2.3.1 Airfoil Self-Noise

Airfoil self noise is created by the interaction between the airfoil and its boundary layer. In general, an airfoil operates in three boundary layer conditions: laminar, turbulent and separation (or stall). The self-noise produced in these cases is caused by different mechanisms, and is best described by the work of Brooks *et al.* [6]. The formal names of these self noise mechanisms are Turbulent Boundary Layer - Trailing Edge (TBL-TE), Laminar Boundary Layer - Vortex Shedding (LBL-VS) and separation-stall, seen in Figure 2.4 as (a), (b) and (d), respectively. In addition, a blunt trailing edge generates noise through vortex shedding, and tip vortex noise is caused by the fluctuating pressures caused by the

formation of tip vortices in a 3D situation. The key airfoil self-noise mechanisms for wind turbines are TBL-TE and LBL-VS, which occur depending on the design of the turbine.

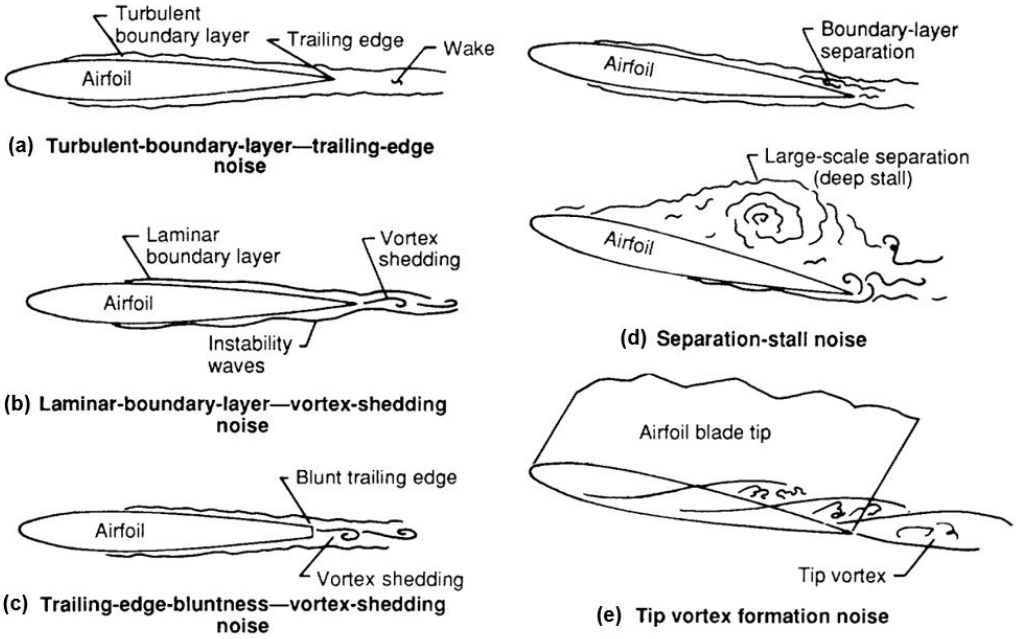

Figure 2.4: Airfoil self-noise mechanisms. Adapted from Brooks *et al.*[6]

The LBL-VS mechanism creates broadband noise with tonal components in small scale wind turbines where the chord Reynolds Number, Re, is between 10^5 and 10^6 as stated by Wagner *et al.* [5]. The source of the tonal noise was thoroughly investigated in the 1970's, including work from Paterson *et al.*. [7], Tam [8], Fink [9], and Wright [10]. Arbey and Bataille [11] conducted studies and confirmed the theory proposed by Fink, in which the tonal noise is created by Tollmien-Schlichting (T-S) waves. These instability waves are triggered when sound waves radiate upstream from the trailing edge, creating a feedback loop capable of producing sharp tonal noise. The sound producd by this mechanism can be described as a whistling noise, and is best mitigated by tripping the boundary layer to cause turbulent flow, which disrupts the feedback loop [12].

The TBL-TE mechanism creates broadband noise in the outer portion of large, Megawatt (MW) scale, wind turbines where the Re is greater than 10^6 [12]. This mechanism is much less complex than the LBL-VS mechanism, but is difficult to mitigate. The broadband noise produced is described as a swishing sound, and is a result of turbulent eddies passing the trailing edge of the airfoil [5]. These eddies are contained within the turbulent bound-

ary layer, and scatter their energy in the form of acoustic pressure when passing the sharp trailing edge. Current investigations into reducing TBL-TE noise involve either modifying the boundary layer interaction at the trailing edge with brushes or saw-tooth serrations, or modifying the boundary layer upstream of the trailing edge by blowing air from within the blade [13].

2.3.2 Wind Turbine Noise

Modern Horizontal Axis Wind Turbine (HAWT)s can be divided into two major groups, MW scale and small scale. MW scale turbines are the large turbines used in commercial wind farms, with power production ranging from around 1 MW to 12 MW for the newest offshore turbines [14]. These turbines largely experience the TBL-TE self-noise mechanism and therefore emit broadband noise. The majority of the noise is generated at the trailing edge of the blade, and in the third of the blade closest to the tip. This portion of the blade has the highest relative wind velocity and therefore is most likely to be operating with a turbulent boundary layer. Figure 2.5 shows the acoustic source map for a MW scale wind turbine with acoustic sources at the hub of the turbine (the centre of rotation) and the right half of the blade's rotation [15]. The sound from the hub is due to the generator and other mechanical components housed inside. The aeroacoustic noise from the blade is only present on one side for ground level measurements due to the direction that the sound propagates, also known as the directivity, of the TBL-TE acoustic mechanism, which is most effective perpendicular to the trailing edge [12]. Simplifying the airfoil as an infinite flat plate leads to the approximate directivity pattern, shown in Figure 2.6, of $p^2 \propto \sin^2(\theta/2)$ which accounts for TBL-TE noise and also turbulent inflow noise [16]. Therefore the noise can only be heard when the leading edge of the blade is directed towards the ground, which is called the down-sweep of the blade. At all other locations of the rotation, the sound is directed to the atmosphere.

Small scale turbines are used for micro-generation where lower power is required, such as remote communities, small businesses and individual dwelling off-grid use. They operate at lower Re are more likely to experience LBL-VS noise and therefore can have a combination of tonal and broadband noise emitted. Since tonal noise generation by a wind turbine would cause significant annoyance, those in operation are either modified to operate at a higher Re or have a boundary layer trip added. For this reason, small scale turbines usually experience TBL-TE noise and acoustic source maps strongly resemble those of MW scale wind turbines, as seen in Figure 2.7.

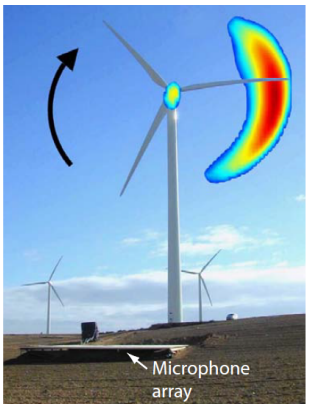

Figure 2.5: Acoustic source map of a Gamesa G58 turbine ($0.85MW$) by Oerlemans *et al.* using a microphone array [15]

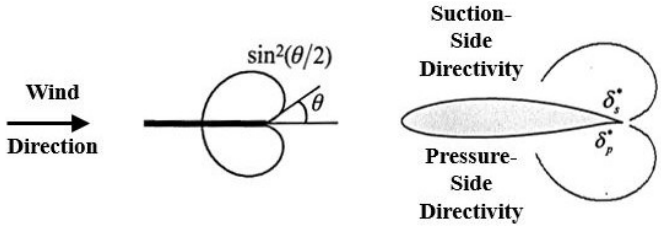

Figure 2.6: Directivity for an infinite flat plate (left) and 2D airfoil (right). Modified from Oerlemans [12].

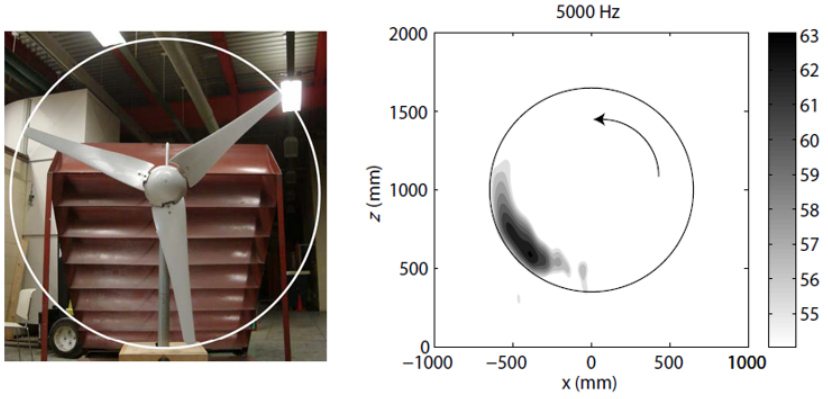

Figure 2.7: Acoustic source map of a small wind turbine by Bale using a MEMS microphone phased array [17]

2.4 Aeroacoustic Prediction Models

The understanding of aeroacoustic noise for airfoils comes from the desire to predict and reduce the noise generated by airplanes, helicopters and wind turbines. These predictions can be split into two general groups, semi-empirical models and fully analytical models. The main difference being that semi-empirical prediction requires experimental data for the airfoil and fully analytical models rely solely on the fundamentals of fluid dynamics and acoustics. Semi-empirical models are faster and less computationally expensive for airfoils that already have experimental data, but cannot reliably predict noise from new designs. Fully analytical models are capable of predicting the noise for any airfoil design and configuration, but the prediction can be limited by the computational resources available. The following sections outline the current semi-empirical and fully analytical models used in literature.

2.4.1 Semi-Empirical Models

Semi-empirical models are developed through investigation of large data sets by replicating trends in mathematical models. Today, semi-empirical models are dominated by a combination of two models: Amiet's model for turbulent inflow noise [18], and the Brooks, Pope and Marcolini (BPM) airfoil self-noise model [6]. Turbulent inflow noise is caused by the interaction of upstream turbulent eddies with the airfoil, creating broadband noise [5]. Turbulent inflow noise is not discussed in the remainder of this thesis because the simulations replicate experiments conducted in a controlled wind tunnel environment, where incoming turbulence is limited. The BPM model was developed by Brooks *et al.* after conducting a large set of acoustic experiments on the NACA 0012 airfoil, and includes individual prediction models for the airfoil self-noise mechanisms described earlier in this Chapter [6]. This combination of models is used in the NAFnoise program created by the National Renewable Energy Laboratory (NREL) in Colorado and the SILANT program created by a Dutch consortium that consisted of Stork Product Engineering (SPE), the Dutch Aerospace Laboratory (NLR) and the Netherlands Organisation for Applied Scientific Research (TNO) [19] [20].

The NAFnoise program predicts the noise emitted from an airfoil shape, and predicts turbulent inflow noise as well as the noise from the LBL-VS, TBL-TE, blunt trailing edge and separation self-noise mechanisms [21]. Since this program creates a prediction for a 2D airfoil, it is unable to predict the tip noise generated for a given geometry. The turbulent inflow noise calculation is modified from Amiet's model by Guidati to simplify

the turbulent inflow calculation with the use of boundary layer properties from XFOIL [22] [23] [24]. The accuracy of the results are not guaranteed, and can vary depending on the similarities and differences of the submitted airfoil shape to those used in the development of the base models.

The SILANT program outputs noise prediction for an entire wind turbine, by breaking the blade down into segments and combining the results for a full blade prediction that is then propagated to a receiver location[20]. SILANT uses the modification to Amiet's model proposed by Lowson, which is more accurate for wind turbine applications [25].

As mentioned previously, these models require large sets of experimental data and are only applicable to airfoil profiles similar to those used in the creation of the model. New airfoil shapes or noise reduction technologies for wind turbines require fully analytical models to get an accurate aeroacoustic prediction.

2.4.2 Fully Analytical Models

The following is a summary of the development of the FW-H model, including the assumptions and simplifications made during the derivation. The equations used for this research are those in the built-in FW-H model in ANSYS Fluent and an explanation of this model can be found in Section 3.4 [26].

Fully analytical models are capable of predicting the aeroacoustic noise from the fluid flow without the use of experimental data. This field of study is known as CAA and predicts the propagation of acoustic waves caused by pressure disturbances in the flow. CAA methods require the flow field solution from a CFD simulation, steady or transient, to serve as the source for the acoustic propagation. The solution method can be divided into two main subcategories: direct computation and acoustic analogy. Direct computation requires the simultaneous solution of the flow field using a CFD method and has strict solution requirements to maintain minimal numerical dispersion and dissipation as well as extremely fine mesh sizing requirements between the source and the receiver [27]. An acoustic analogy simplifies the CAA solution by assuming that a bounded region in the flow can be solved as an acoustic source and then linearly propagated in the surrounding area using the general wave equation [28]. It has been well established by those in the CAA field that for low Mach number flows and flows where the propagation distance is large, acoustic analogy is a better option when compared to direct computation, especially when considering rotating flows such as helicopters [28] [29]. Since wind turbine aeroacoustics resembles the general setup of helicopter rotor noise prediction, this research focuses on the

application of the FW-H equation, which was modified from the acoustic analogy proposed by Lighthill in his theory of aerodynamic sound [30].

The basis of all acoustic prediction is the linear wave equation which is derived from a combination of the conservation of mass, momentum and energy, more commonly known as continuity, Euler equations and Navier-Stokes, and the energy equation, respectively [5]. The elementary solutions of the wave equation are known as monopoles and dipoles, which are obtained by applying the method of Green's functions [5]. Monopoles are described as sources of fluid, where fluid is either added or removed, and produce a uniform distribution of sound. Dipoles are a result of a fluctuating force field in part of the medium, and produce a two-lobed directionality pattern. These source patterns can be seen in Figure 2.8.

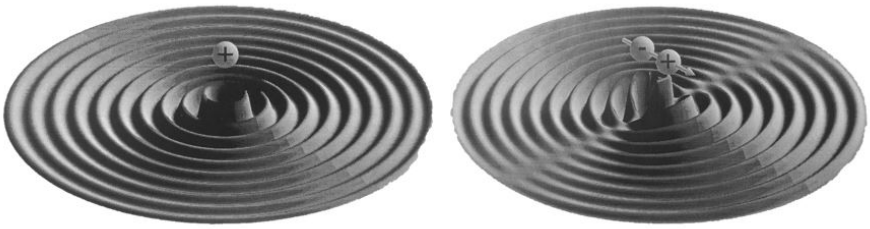

Figure 2.8: Instantaneous sound waves for a monopole (left) and dipole (right) source as shown by Wagner *et al.* [5]

Lighthill's acoustic analogy applies continuity and Navier-Stokes to a bounded region that contains a turbulent flow. Equation (2.6) and (2.7) show the rearrangement of these equations into an inhomogeneous wave equation, where the forcing term contains Lighthill's Tensor, T_{ij}, a tensor representing viscous stresses and fluctuating Reynold's stresses [30]. A simplification of Lighthill's tensor (Equation (2.8)) can be applied in turbulent flows, where the fluctuating Reynold's stresses dominate and therefore viscous stress terms can be neglected [5]. This analogy allows for computation of acoustic sources within the bounded turbulent flow, and propagates the resulting waves through the area of flow that is free from acoustic pressure and density fluctuations [5]. This analogy introduces a new source of aerodynamically generated noise: the quadrupole source, which can produce a distribution pattern similar to the two-lobed dipole pattern, or a four-lobed pattern [30].

$$\frac{\partial^2 \rho'}{\partial t^2} - c_o^2 \frac{\partial^2 \rho'}{\partial x_i^2} = \frac{\partial^2 T_{ij}}{\partial x_i \partial x_j} \tag{2.6}$$

$$T_{ij} = \rho u_i u_j + \left(p - p_0 - c_0^2(\rho - \rho_0)\right)\delta_{ij} + \mu\left[-\frac{\partial u_i}{\partial x_j} - \frac{\partial u_j}{\partial x_i} + \frac{2}{3}\left(\frac{\partial u_k}{\partial x_k}\right)\delta_{ij}\right] \tag{2.7}$$

$$T_{ij} = \rho u_i u_j = \rho \begin{pmatrix} u_1^2 & u_1 u_2 & u_1 u_3 \\ u_2 u_1 & u_2^2 & u_2 u_3 \\ u_3 u_1 & u_3 u_2 & u_3^2 \end{pmatrix} \tag{2.8}$$

Lighthill's analogy was developed for predicting the aeroacoustic noise from jets, and has a restriction that the flow must be unbounded and therefore is not applicable to flows around a body. This led to several extensions of Lighthill's theory, first by Curle considering the influence of static surfaces and then by Ffowcs-Williams and Hawkings to include surfaces in arbitrary motion [31]. The surface is incorporated into the analogy by creating a function that describes its shape and motion, and then using the Dirac delta function to establish when to apply the surface-related terms to the acoustic prediction [31]. A visualization of this procedure is shown in Figure 2.9. The FW-H equation includes all the terms present in Lighthill's analogy, with two additional terms added, which are in the form of monopole and dipole sources of noise [31]. The resulting equation has three inhomogeneous terms: a quadrupole term which accounts for sound generated by fluctuating Reynolds stresses, a monopole (or thickness noise) term and a dipole (or loading noise) term. Together, the thickness and loading noise terms represent the sound generated by the body passing through the flow [5]. In Equation 2.9, the quadrupole term contains Lighthill's Tensor, T_{ij}, the loading noise term contains the compressive stress tensor, p_{ij}, and the thickness noise term contains the fluid velocity, u_i [31].

$$\left(\frac{\partial^2}{\partial t^2} - c_o^2\frac{\partial^2}{\partial x_i^2}\right)(\rho' H(f)) = \frac{\partial^2}{\partial x_i \partial x_j}(T_{ij}H(f)) - \frac{\partial}{\partial x_i}\left(p_{ij}\delta(f)\frac{\partial f}{\partial x_j}\right) + \frac{\partial}{\partial t}\left(\rho_0 u_i \delta(f)\frac{\partial f}{\partial x_i}\right) \tag{2.9}$$

The function, $f(\overrightarrow{x}, t) = 0$, defines the surface of the body and therefore the quadrupole term applies outside of the defined surface, and the thickness and loading noise terms only apply on the surface of the body. In the case of airfoil self-noise, the quadrupole term is often neglected since the noise generation is dominated by the thickness and loading noise terms [32]. Farassat determined the general solution for the monopole and dipole terms added by Ffowcs-Williams and Hawkings, and his updated form of the solutions are those applied by ANSYS Fluent [32].

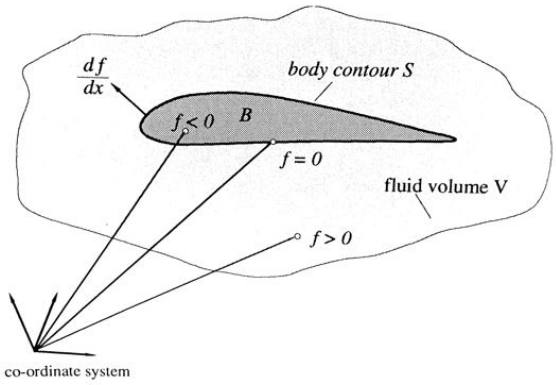

Figure 2.9: Example of surface function, f, for body, S, where calculation of noise sources occurs when $f = 0$ as shown by Wagner *et al.* [5]

A limitation of Lighthill's analogy and the FW-H equation is that it applies to regions that are acoustically compact. Acoustical compactness is a condition where a source region of size l must have acoustic wavelengths, λ, that are much larger in length [31]. This condition simplifies the calculation of volume integrals of the bounded region, since it allows the neglecting of differences in retarded time within the source [5]. The retarded time, τ, is used to define the time an acoustic wave was generated to be able to reach the observer at time, t [5].

2.5 Aeroacoustic Research in Literature

This section summarizes the relevant research conducted in the fields of fluid dynamics and aeroacoustics, including both experimental and computational work. The experimental data serves as a comparison for the simulated results to determine the accuracy of the CFD simulation and the effectiveness of the aeroacoustic prediction method for wind turbine applications. The summary of computational research outlines previous successes in this field and summarizes best practices for setting up accurate simulations.

2.5.1 Experimental Data

The experimental data in literature can be divided into two categories: fluid dynamics and aeroacoustics. The two airfoils used in this research are NACA 0012, which is a

standard symmetric airfoil that has been used widely for experiments, and SD 7037, which is a cambered airfoil designed specifically for low Re wind turbines. The latter is not common in experimental research, but studies exist for similar airfoils which serve as valid comparisons. The airfoil profiles for SD 7037 and NACA 0012 are shown in Figure 2.10, and also shows the coordinate system used, and the definition for the Leading Edge (LE), Trailing Edge (TE) and chord length, c.

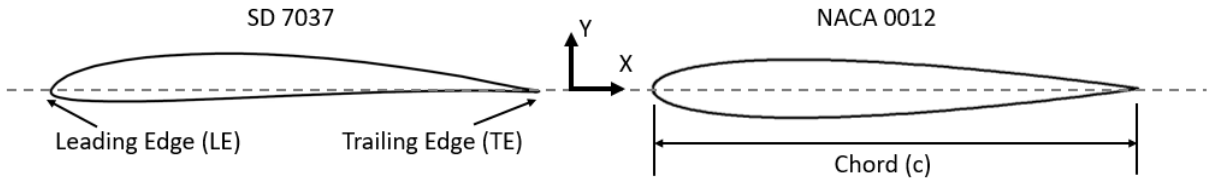

Figure 2.10: SD 7037 and NACA 0012 airfoil profiles

The acoustic data for the NACA 0012 airfoil was collected by Brooks *et al.* [6] for the development of the BPM semi-empirical model mentioned in Section 2.4.1. The model required a significant number of experiments on the NACA 0012 airfoil at different static AOAs, chord lengths and trailing edge conditions. These experiments were conducted in an anechoic open jet wind tunnel, and have been referenced extensively since they were published. Results relating to the flow around the NACA 0012 airfoil are well known and come from several sources. The lift and drag data for the simulated Re was reported by Abbott and Von Doenhoff in the 1959 book Theory of Wing Sections [33]. Experimental pressure coefficient data was published by Gregory and O'Reilly in a 1970 report on the aerodynamic characteristics of the NACA 0012 airfoil [34].

The results for the SD 7037 airfoil all come from research of the Wind Energy Group at the University of Waterloo, and all experiments were conducted in a closed loop wind tunnel with the same airfoil and tunnel test section dimensions. The flow results were gathered through Particle Image Velocimetry (PIV) measurements and surface oil flow visualization conducted by Ghorbanishohrat [2]. Ghorbanishohrat's work investigates the boundary layer and LSB behaviour of the static and dynamic SD 7037 airfoil, and produced high quality images of the flow field, as well as pressure coefficient data along the chord of the airfoil [2]. In 2017, Tam published a study on airfoil self-noise for wind turbine applications which included acoustic measurements on a SD-7037 airfoil [35]. These measurements were taken at both static and oscillating AOAs to understand the aeroacoustic noise under the dynamic conditions wind turbines operate in when installed. The experimental setup is shown in Figure 2.11.

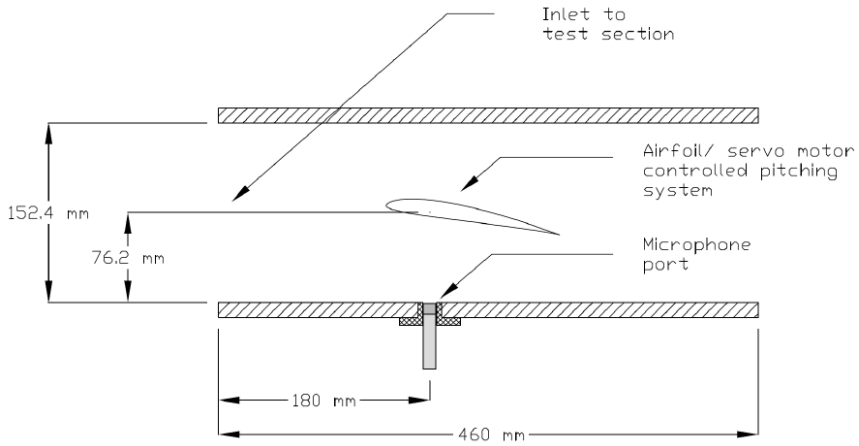

Figure 2.11: SD-7037 test setup for Tam experiments [35]

2.5.2 Computational Aeroacoustics

Computational simulations using LES and the FW-H analogy were conducted by Wolf *et al.* in 2012 to replicate the Brooks *et al.* NACA 0012 experiments for $Re = 4.8 \times 10^5$ [36]. The work largely focused on the impact of the quadrupole sources on airfoil acoustics, and concluded that for low Mach number flows, the quadrupole sources are not required. They stated that compressible LES is required to determine the accurate pressure fluctuations on the surface of the airfoil, since insufficient near wall resolution combined with the incompressible LES simulation was not sufficient in previous work.

More recently, computational simulations of the noise produced by blade segments and full turbine blades were conducted by Wasala [37]. The major focus of the simulations was to predict the noise reduction from leading edge owl hooks, which disrupt the TBL-TE acoustic generation mechanism [37]. Before adding noise reduction technologies, the results from Brooks *et al.* for NACA 0012 at $Re = 1.5 \times 10^6$ were replicated using incompressible LES and FW-H. The geometry for the Brooks *et al.* replication simulations are shown in Figure 2.12.

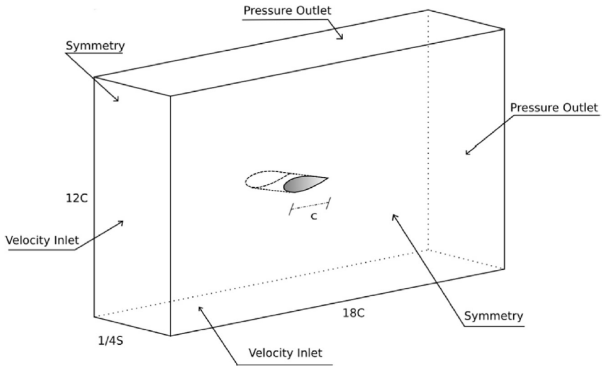

Figure 2.12: Wasala simulation geometry for NACA 0012 aeroacoustic simulations [37]

2.6 Summary

This chapter covered the important background information required for understanding the theory behind the computational aeroacoustic study of airfoils. Though the application of CAA models extends to many areas of research, the focus of this thesis is the prediction of wind turbine noise. The fluid dynamics principles for wind turbine operation and airfoil boundary layer theory explain the flow conditions expected over wind turbine blades. Acoustic theory and its relationship with airfoil self-noise helps to understand the acoustic behaviour of small and large scale wind turbines. The current aeroacoustic prediction models were summarized, including the derivation of the FW-H model used in this thesis. Finally, the relevant experimental and computational research on the NACA 0012 and SD 7037 airfoil was included to highlight the data used for comparison in the results chapters.

Chapter 3

CFD and CAA Models

This chapter describes the analytical models used for the prediction of aeroacoustic noise, which includes CFD and CAA theory. The CFD portion of the simulation involves a combination of Reynolds-Averaged Navier-Stokes (RANS) and LES, with an optional use of the energy equation to solve the compressible flow field. The CAA model used is FW-H, and is computed simultaneously with the energy equation and LES to produce the aeroacoustic noise prediction. All simulations were run using the built-in models of ANSYS Fluent, Release 18; no User-Defined Functions (UDF) were used [38]. Acoustic data was post-processed using MATLAB version R2018b [39].

3.1 Energy Equation

The energy equation is a fundamental equation in fluid dynamics, and is derived from the first law of thermodynamics [40]. The energy equation is used in conjunction with either RANS or LES to include the effects of density and temperature in the flow. It is typically not used for incompressible external flow simulations, but using the energy equation with the ideal gas law selected for fluid density calculation results in a compressible flow solution and increases the accuracy of the results [36]. When solving compressible flows with strong acoustic pressure fluctuations, the non-reflecting boundary condition is required to prevent the reflection of acoustic waves [27]. This option is specifically for acoustic pressure waves since they dissipate much slower than pressure waves caused by regular flow behaviours and therefore the selected far field boundaries are not sufficient to prevent reflection.

3.2 Reynolds-Averaged Navier-Stokes (RANS)

The RANS model was used to initialize the pressure and velocity field and provide an accurate starting point for the LES simulation, as per the recommendation in ANSYS Fluent [26]. Since this model is used for the initialization of the flow, the model parameters used are not important as long as a converged solution is reached for the given mesh and boundary conditions. The basic principle of the RANS model is to separate the flow variables of the Navier-Stokes equations into mean and fluctuating components, which creates separate terms, called Reynolds stresses ($-\rho\overline{u_i' u_j'}$), responsible for representing the turbulence in the flow [26]. The Reynolds stresses are modelled using the Realizable $k-\epsilon$ model, which improves on the original $k-\epsilon$ two equation turbulence model by using an alternative formulation for the turbulent viscosity and a modified transport equation for the dissipation rate [26]. This results in a model that better simulates stronger vortices and rotation in the flow, which provides a more accurate starting point for the LES simulation. The RANS model is for steady-state simulations and is unable to simulate the vortex shedding from the trailing edge of the airfoil, meaning the LES simulation still requires a start-up period before reaching a statistically steady solution.

3.3 Large Eddy Simulation (LES)

The LES model was used for the transient solution of the flow field and uses the RANS simulation data as an initialization. The model applies the time- dependent Navier-Stokes equations to the domain while using filters to remove eddies smaller than the grid spacing [26]. The large eddies are more strongly dependent on the geometry of the problem and therefore require the application of the Navier-Stokes equations. The small eddies are less dependent on the geometry of the problem and therefore have more predictable behaviour that can be solved using a subgrid-scale model which determines the subgrid-scale turbulent viscosity, μ_t. The model chosen for this research is the Dynamic Smagorinsky-Lilly Model, which determines the mixing length for the subgrid scale with the use of the Smagorinsky constant, C_s, which is dynamically computed using a test filter length that is twice the size of the grid spacing [26]. The use of LES requires finer mesh sizing and higher computational cost than RANS simulation but allows for a coarser mesh and larger time step sizing than a Direct Numerical Simulation (DNS) [26]. The LES simulation of the flow can provide high accuracy transient data without requiring a computationally expensive DNS solution, and is therefore an optimum method for predicting the surface pressure data required for the FW-H model.

3.4 Ffowcs-Williams and Hawkings (FW-H) Acoustic Model

The development of the FW-H equation was described in Section 2.4.2, and in this section, the solution and its use in Fluent is explained. The solution of the FW-H acoustic analogy used for this model is Formulation 1A by Farassat, which places an impermeable surface on the airfoil and calculates the sound propagation using a retarded time frame [32]. The total noise, in acoustic pressure (p), produced by a surface in the flow is calculated using Equation 3.1, which combines the monopole (thickness, p_T), dipole (loading, p_L) and quadrupole, p_Q, noise sources together. Farassat's solution for the thickness and loading noise terms and the solution for the quadrupole term for Formulation 1A can be found in the work by Farassat and Brentner [41][42].

$$p'(x,t) = p'_T(x,t) + p'_L(x,t) + p'_Q(x,t) \tag{3.1}$$

ANSYS Fluent has a built-in FW-H solver that applies Formulation 1A in a similar way to that described by Farassat. The main difference is the solution uses a semi-permeable surface that can be offset from the airfoil to compute the quadrupole noise for the flow contained within the surface [26]. However, when placed coincident to the airfoil surface, the calculation simplifies to the Formulation 1A solution. The latter method was used for the prediction model.

3.5 Summary

This chapter summarized the analytical models used for the simulations, which are all built-in to ANSYS Fluent. RANS was used as initialization for the flow field, and then LES and the FW-H acoustic analogy were applied to solve for the transient solution. Simulations that were solved as compressible flows utilized the energy equation along with the ideal gas calculation of the fluid density.

Chapter 4

Numerical Setup

The goal of the numerical simulations was to generate an accurate acoustic prediction for the given airfoil and flow conditions. Three models were required: RANS to initialize the flow field, LES to simulate the flow field to obtain the unsteady pressure and velocity data, and FW-H to determine the propagation of acoustic pressure waves. These models were applied to a structured C-Mesh control volume for two different airfoils. Case 1 and Case 2 use the NACA 0012 airfoil and though were initially intended for validation purposes, serve as their own set of results. These cases use the geometry and experimental results of Brooks *et al.* [6] and follows the general parameters of the work by Wasala [37]. The remaining cases use the SD 7037 airfoil geometry from the experimental results of Ghorbanishohrat [2] for flow and Tam for acoustics [35]. The general information for the 6 test cases is summarized in Table 4.1. This chapter summarizes the specifics of the numerical models used, as well as the geometry and mesh required.

Parameter	Case 1	Case 2	Case 3	Case 3a	Case 4	Case 4a
Airfoil	NACA 0012	NACA 0012	SD 7037	SD 7037	SD 7037	SD 7037
Mesh Type	Coarse	Fine	Coarse	Coarse	Coarse	Coarse
Compressible	No	No	Yes	No	Yes	No
Angle of Attack (°)	0	0	0	0	1	1

Table 4.1: Simulation Cases

4.1 Geometry and Mesh

The dimensions of the NACA 0012 case and the SD 7037 case differ greatly and also experience different types of flow. Both can be considered low Mach number flows, and are well below Mach 1, which indicates that an incompressible flow solution should be sufficient. The NACA case is considered a high Reynolds number flow, while the SD case is a low Reynolds number flow. This presents challenges for simulating the SD case since low Re cases are more likely to have complex feedback structures in the boundary layer. The geometry and meshing strategy for both cases are the same and apply a structured C-Mesh with tightly controlled inflation at the surface of the airfoil. The key parameters of the simulated geometries are shown in Table 4.2, while a more in-depth explanation of the meshing can be found in the following sections.

Parameter	NACA 0012	SD-7037
Chord (m)	0.3048	0.025
Span (m)	0.1143	0.150
Domain Width (m)	0.1143	0.01028
Domain Height (m)	7.315, 3.048	1.000, 0.6
Domain Length (m)	7.315, 3.048	1.000, 0.6
Velocity (m/s)	71.3	24.8
Re	1.5×10^6	4.25×10^4
Ma	0.21	0.073
Receiver (m above airfoil)	1.219	-0.0762

Table 4.2: Simulation Geometry Parameters

4.1.1 NACA 0012

The NACA 0012 geometry is dependent on the chosen control volume since the reported experiments were performed in an open-jet wind tunnel and have no physical limitations on the surrounding flow [6]. The chord length, velocity and receiver dimensions originate from the Brooks *et al.* experiments [6]. The other dimensions specify the control volume size, and roughly follow the values given by Wasala [37]. Wasala chose to simulate the flow using a rectangular control volume, but for these simulations a C-type control volume was chosen to achieve better mesh quality on the leading edge portion of the airfoil. The structured mesh was achieved by creating sub-parts in the geometry that allowed for rapid

inflation at the surface of the airfoil, and a slower expansion towards the inlet and outlet, as seen in Figure 4.1. The airfoil surface is accurately represented by 200 chordwise divisions on the pressure and suction sides, and 50 spanwise divisions. The mesh was created to keep the Courant Number (CFL) less than one and also $y^+ < 1$ for the airfoil surface with the value reaching 1.5 adjacent to the stagnation point at the leading edge of the airfoil [43]. The mesh has a total of 3 million cells, and uses boundary offsets of 12 chord lengths to ensure all inlets and outlets experience free stream pressure and velocity.

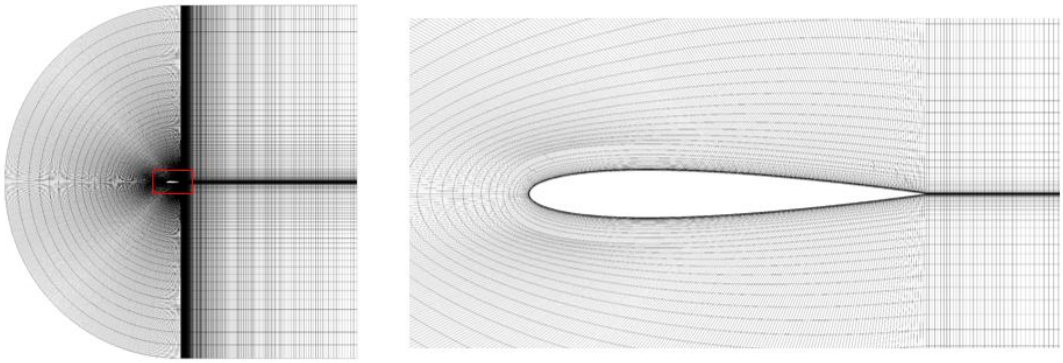

Figure 4.1: Case 1 C-Mesh for NACA 0012 with box indicating airfoil close-up

A second variation of this mesh was created to determine the impact of increasing the number of elements in the region between the surface of the airfoil and the receiver location. This dense region of nodes, shown in Figure 4.2, was added by creating new sub-parts in the geometry between the inflation region and the location of the microphone in the flow. The mesh spacing in this region was fixed (no inflation) and approaches the 18 to 25 mesh points per wavelength recommended by Tam for direct CAA simulations [27]. Though this simulation uses a CAA model instead of direct CAA, this guideline was followed to aid in the simulation of the flow around the airfoil to attain better surface pressure fluctuation results. Based on the target frequency range of 0.5 to 10 kHz in the experimental data, the mesh spacing was selected as 16 nodes for the 10 kHz wavelength and resulted in a mesh spacing of $2.26 \times 10^{-3} m$. Due to limitations of the computer used for post-processing, the offset of the boundaries were reduced from 12c to 5c to keep the number of elements at the manageable amount of 17 million.

Case 1 and 2 use the same boundary conditions since they are at an identical AOA and free stream velocity. The curved and horizontal surfaces of the control volume are set as velocity inlets with the velocity, U_∞, set at $71.3 m/s$ in the x-direction for 0° AOA. Inlet turbulence was introduced using the spectral synthesizer provided by Fluent, with the

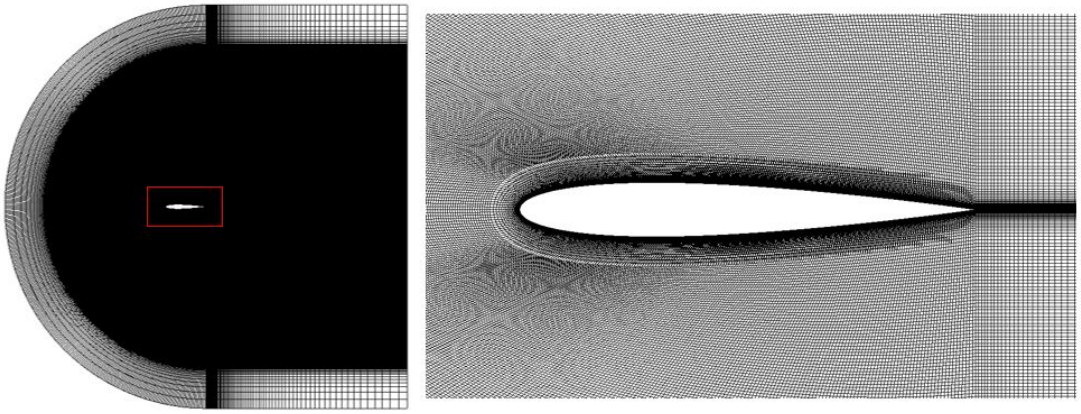

Figure 4.2: Case 2 C-Mesh for NACA 0012 with box indicating airfoil close-up

turbulent intensity set at $I = 0.4\%$ and the length scale set at $l = 0.003m$ to recreate the inlet turbulence conditions of the tunnel in which Brooks *et al.* conducted their experiments [37]. The downstream exit boundary was set as a pressure outlet with a gauge pressure of $0Pa$. The vertical faces at either end of the airfoil span were set as symmetry, and the airfoil surface was set as a no-slip wall. These boundary conditions are shown in Figure 4.3.

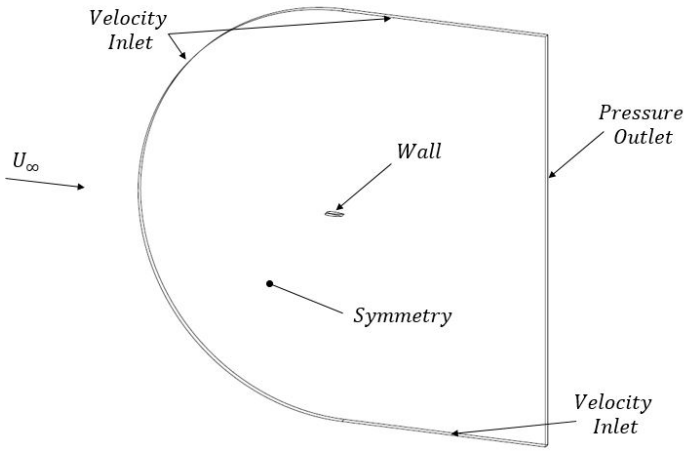

Figure 4.3: NACA 0012 Case 1 and 2 boundary conditions

4.1.2 SD 7037

The experimental geometry for the SD 7037 cases is as shown in Figure 2.11, where a $25mm$ chord airfoil with a span of $152.4mm$ was placed in a closed loop wind tunnel with a square test section of $152.4mm \times 152.4mm$. The geometry for the simulations is a C-Mesh and a span 1/15 of the experimental span. As with the NACA 0012 simulation, the geometry and mesh differ between the cases. For Case 3 and 4, the compressible cases, the boundary offsets are 20 times the chord length, and for Case 3a and 4a, the incompressible cases, the boundary offsets are 12 times the chord length. To avoid discrepancies between the simulated and experimental Sound Pressure Levels (SPL), 15 microphones were added to the simulation as shown in Figure 4.4 to gather an acoustic signal that represents the entire span of the experimental airfoil.

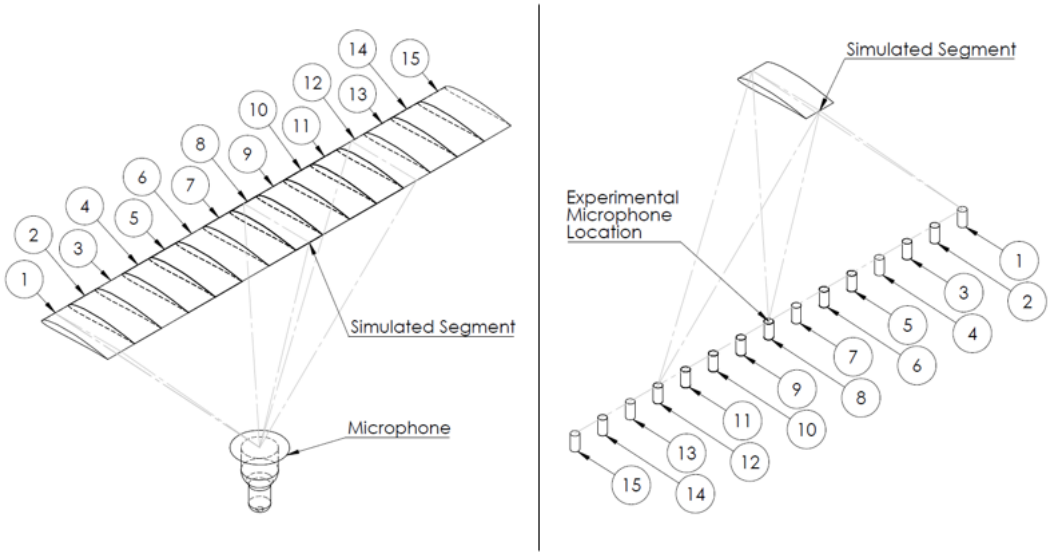

Figure 4.4: SD-7037 Relative microphone locations for simulation setup

The mesh does not include the tunnel walls as the effects are assumed negligible on the flow behaviour around the airfoil. The mesh was broken down into three sections to accurately simulate: (a) the boundary layer and wake of the airfoil, (b) the area between the boundary layer and the microphone, and (c) the far field (Figure 4.5a). The boundary layer segment is set up such that $y^+ < 1$, 8 to 10 elements are within the boundary layer and there is a smooth transition to the outer mesh [43]. The mesh spacing between the boundary layer inflation and the microphone location was kept at a constant spacing in the mesh for Case 3 and 4 to maintain the direct CAA recommendation of 25 nodes

per wavelength for the frequency range of $1.6kHz$ to $8kHz$ [27]. The mesh for Case 3a and 4a does not have this region, but due to the small geometry of the SD 7037 case in comparison to the wavelengths required, the mesh has at least 9 nodes per wavelength between the airfoil and the receiver. The far field area allows for expansion of the mesh while maintaining realistic aspect ratios. The mesh has a total of 7 million cells for Case 3 and 4, and 2.4 million cells for Case 3a and 4a, and to ensure accurate simulation of the pressure fluctuations on the surface of the airfoil, there are 200 nodes along the chord of the airfoil. The mesh for Cases 3 and 4 is shown in Figure 4.5, and the mesh for Case 3a and 4a is shown in Figure 4.6.

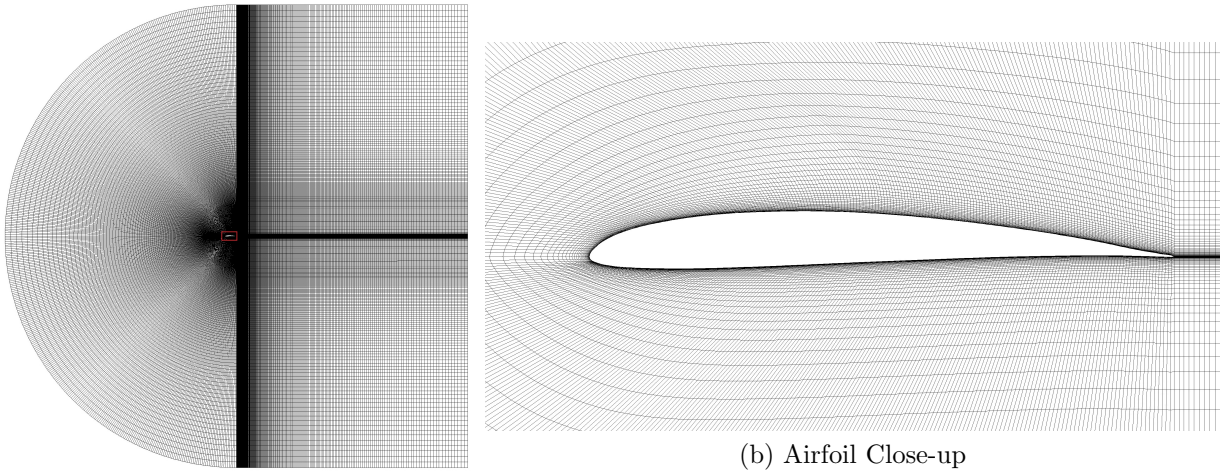

(a) Case 3 and 4 mesh

(b) Airfoil Close-up

Figure 4.5: C-Mesh for SD 7037 Case 3 and 4, with box indicating airfoil close-up view

The inlet for the C-Mesh is specified as the front curved surface as well as the top and bottom horizontal surfaces. The velocity components are set for the given angle such that the velocity magnitude is $24.8\cos\theta$ m/s in the x-direction and $24.8\sin\theta$ m/s in the y-direction, with a turbulent intensity of 1.23% and length scale of $0.0107m$ [35]. The downstream exit boundary is set as a pressure-outlet. Both the inlet and outlet have the Non-Reflecting condition set for the acoustics model. The side surfaces are set as symmetry and the airfoil surface is set as a non-slip wall. This is the same boundary condition setup as shown in Figure 4.3 for the NACA 0012 cases.

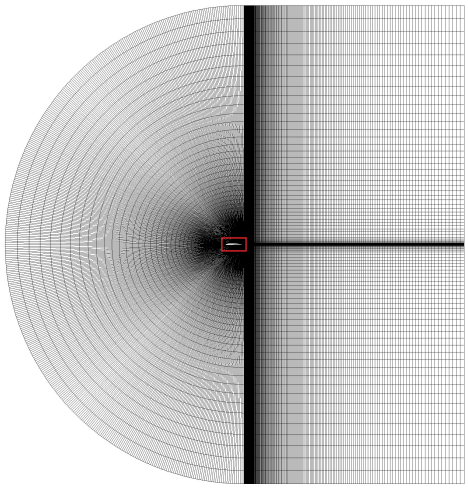

(a) Case 3a and 4a mesh

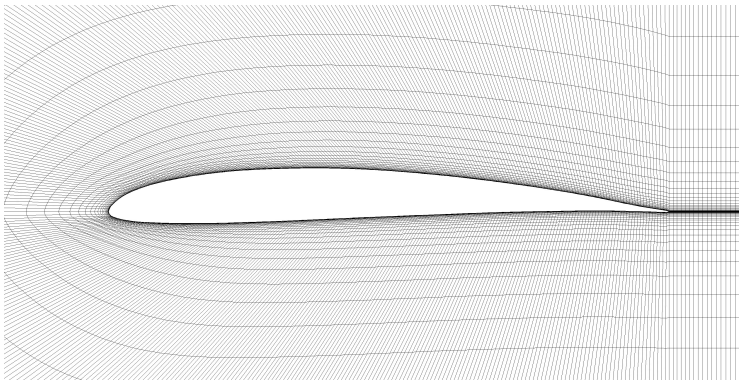

(b) Airfoil Close-up

Figure 4.6: C-Mesh for SD 7037 Case 3a and 4a, with box indicating airfoil close-up view

4.2 Solver Setup

The RANS initialization was run with the realizable $k - \epsilon$ model, with standard wall functions. The pressure-velocity coupling scheme used was SIMPLEC with Second Order Upwind spatial discretization. Convergence criteria was set at 1×10^{-6} for all residuals. After convergence was achieved, the instantaneous flow field was generated using the built in Fluent command init-instantaneous-vel [26].

For the transient solution, Fluent's built in models for LES and FW-H were activated, and for the compressible flow cases, the energy equation and ideal gas calculation of the air density were initiated [26]. The LES subgrid-scale model was chosen as Dynamic-Stress Smagorinsky-Lilly. The acoustics model defined the source as the surface of the airfoil and the receiver locations as those listen in Table 4.1 for the NACA 0012 cases or shown in Figure 4.4 for the SD 7037 cases. The acoustic data was exported at each timestep and calculated after the completion of the transient simulation, rather than calculating the full acoustic propagation at the end of each time step. The time step was set at $1 \times 10^{-6} s$ and convergence criteria for all residuals was set at 1×10^{-6} for Case 1, 5×10^{-7} for Case 2, and 5×10^{-5} for the SD 7037 Cases. As with the RANS initialization, the SIMPLEC scheme was used, with Second Order discretization for pressure and Bounded Second Order Implicit for the transient formulation. The solution was run for one Mean Flow Residence Time (MFRT) for the NACA 0012 cases and 2 MFRTs for the SD 7037 cases to allow for

the generation of a statistically steady solution. Solution behaviour was gauged by the monitoring of residuals, lift and drag coefficient files that were output for each timestep and the number of iterations per timestep. After an initial transient period, the iterations per timestep levelled off at 5 for Case 1 and 2, 7 for Case 3 and 4, and 10 for Case 3a and 4a, which all indicate a good balance between computing time and solution accuracy [43].

The RANS and LES simulations were performed using the high performance computer cluster Graham, which is a part of the SHARCNET network and the greater Compute Canada network [44] [45]. The simulations were generally run using one complete node of the system, which contains 32 cores and required 3.25 weeks of execution time, or 1 month when including wait times for resources, to meet desired MFRT goal. The FW-H results, post-processing and graphics were performed in Fluent on a local computer with 8 cores and 32GB RAM.

4.3 Acoustic Processing

Matlab was used to perform the processing of the acoustic signal produced by the FW-H model in Fluent. Before the FFT, a bandpass filter and Hamming window were applied to improve the accuracy of the FFT for the frequency range of interest. After the FFT was applied, the acoustic pressure results for each frequency bin was converted to SPL to determine the narrowband spectra and also summed according to the 1/3 octave band bins for a summary of the acoustic trends. For the SD 7037 cases, the narrowband SPL results for the 15 receivers were added together to find the total noise from the airfoil span. The total narrowband results were used for the 1/3 octave band calculation. The code for this can be found in Appendix A.

4.4 Summary

This chapter covered the numerical setup for the six simulation cases for the SD 7037 and NACA 0012 airfoils. The domain used for the simulation was a C-mesh with controlled inflation at the surface of the airfoil to ensure accurate simulation of the boundary layer and associated surface pressures required for the acoustic model. The SD 7037 simulation geometry used 15 microphones spaced relative to the simulated airfoil to represent the entire span of the experimental geometry. The solver setup summarized the settings used for each of the applied models and also the solver schemes, time step, convergence criteria

and simulation run times. Also included is an explanation of the acoustic post processing that was conducted in Matlab.

Chapter 5

SD 7037 Simulation Results and Discussion

This chapter covers the results for the SD 7037 simulations, specifically Cases 3, 3a, 4 and 4a (see Table 4.1). It covers the flow results and acoustic results, comparing them with data from PIV experiments and acoustic measurements by Ghorbanishohrat and Tam, respectively [2][35]. The results for these cases are presented together because they share many of the same flow characteristics and highlight the key tone generation behaviour for this airfoil.

5.1 Flow Results

Each of the four cases covered in this chapter produce slightly different flow results, though in general they exhibit common trends. This section outlines those similarities and differences in terms of key flow parameters such as lift and drag coefficients, vorticity magnitude and airfoil surface shear stress. Due to the large amount of data collected for these simulations, these results were specifically selected to emphasize the flow characteristics for the purpose of drawing larger conclusions from the acoustic results in the following section.

5.1.1 Pressure, Lift and Drag Coefficients

A common method for validating a flow simulation is to compare the pressure coefficient, C_p, plot as well as the lift coefficient, C_l, and drag coefficient, C_d against experimental

data. The averaged C_p plot shown in Figure 5.1a compares the results for all four cases with the C_p results processed from the PIV data of Ghorbanishohrat [2]. Case 3 & 3a are both at 0° AOA and Case 4 & 4a are both at 1° AOA. The results for each of the simulated AOAs are very consistent for $0 < x/c < 0.9$, with differences occurring at the trailing edge of the airfoil. The most significant trend in this plot is the alignment of the 0° AOA simulated cases with the 1° AOA experimental data, and that the 1° AOA simulated cases are located between the 1° and 3° AOA experimental data. This likely indicates that there are different 0° AOA locations for the simulations and the experiments, which complicates the comparison between the simulated and experimental data. The benefit of studying the low AOAs for this airfoil at the given Re is that there are large boundary layer changes, so even though the simulated AOAs are only separated by one degree, the results for each case are quite different. This is an important point for this results chapter, and should be kept in mind as comparisons are made between the simulations and both flow and acoustic experimental results.

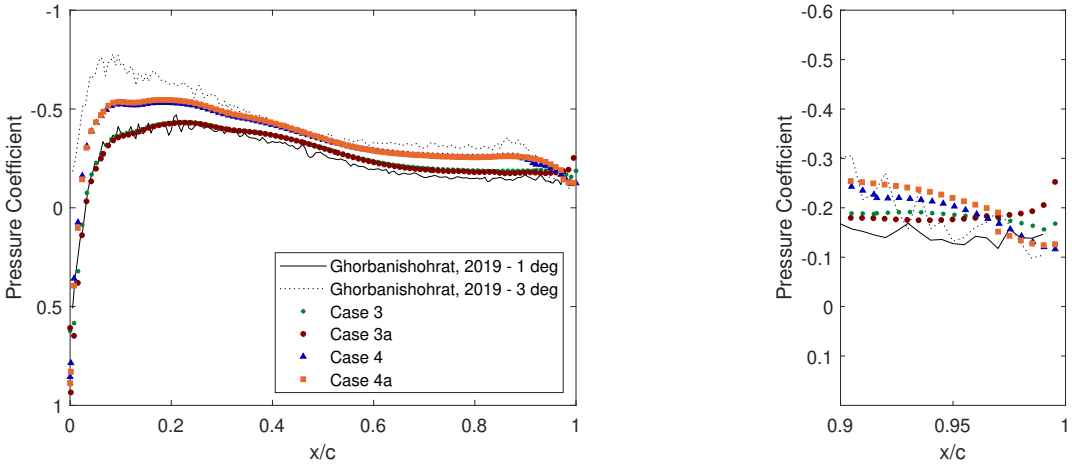

Figure 5.1: Case 3, 3a, 4 and 4a mean pressure coefficient versus x/c compared with experimental data by Ghorbanishohrat [2]. For (a) complete chord (b) $0.9 < x/c < 1$

The compressible and incompressible cases result in slight differences in the trailing edge pressure coefficient behaviour, as shown in Figure 5.1b. Case 3a, the 0° AOA incompressible simulation, shows a much sharper increase in C_p at the trailing edge when compared to the compressible simulation (Case 3). Case 4 and 4a have more consistent results, but both experience sudden jumps in magnitude that occurs at $x/c = 0.92$ for Case 4 and

$x/c = 0.97$ for Case 4a. These behaviours will be explored further in Section 5.1.4 where the boundary layer is analyzed.

The lift and drag coefficients computed for the low AOA cases show good agreement with the trend of the measured PIV data, as shown in Figure 5.2. The compressible simulation, Case 3 and 4, best matches the magnitude for the lift coefficient while the incompressible solutions, Case 3a and 4a, are a better match for the drag coefficient magnitude. The incompressible lift coefficient data aligns better with the experimental data by Selig *et al.*, which is for a higher Re. This comparison serves as a summary for the overall predictive abilities of the simulation, however, the values presented are the mean values and do not take into account the fluctuations of the lift and drag coefficients with time. The time histories of the lift and drag coefficients therefore provide a more in depth look at the transient flow behaviour.

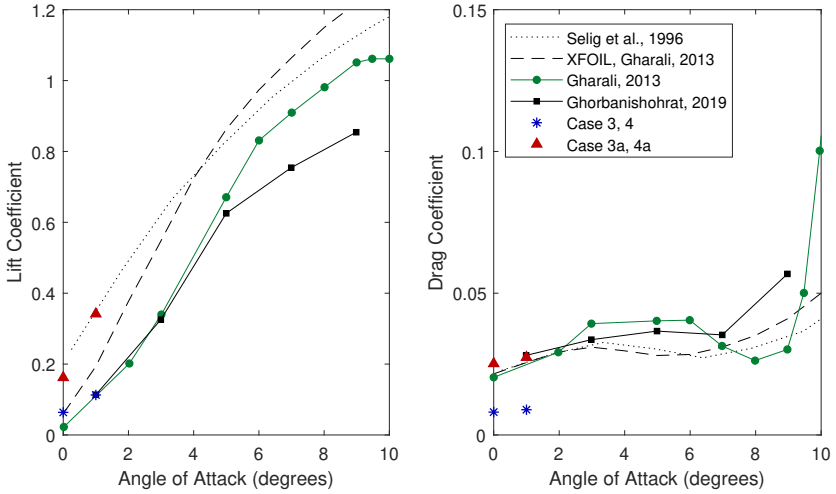

Figure 5.2: Case 3, 3a, 4 and 4a mean lift and drag coefficient values compared experimental data by Selig *et al.* [46] for $Re = 6 \times 10^4$, XFOIL ($Re = 6 \times 10^4$) and PIV results by Gharali [47] and PIV results by Ghorbanishohrat [2]

The lift coefficient time histories in Figure 5.3 reveal some differences in the transient flow behaviour. The amplitude of the lift coefficient is much larger for the incompressible cases when compared to the compressible cases. Figure 5.3b shows that Case 3a has a very regular fluctuation in the lift coefficient indicating a consistent pattern in the boundary layer behaviour, whereas Figure 5.3a shows that Case 3 experiences low amplitude fluctuations of a similar frequency approximately half of the time. Case 3 has these regular

fluctuations when the lift coefficient is below the mean value, and above the mean value exhibits no regular pattern. When comparing Case 3 with Case 4, the amplitudes and low frequency fluctuations appear quite similar, the only major difference is that Case 4 has no regular pattern at any point in the lift history. Finally, Case 4a has a similar pattern to Case 4, but with larger amplitudes for the low and high frequency fluctuations. The differences in the lift behaviour are likely due to higher fluctuations in the velocity at the trailing edge from shed vortices, which would also explain the differences in the TE behaviour in the C_p plot.

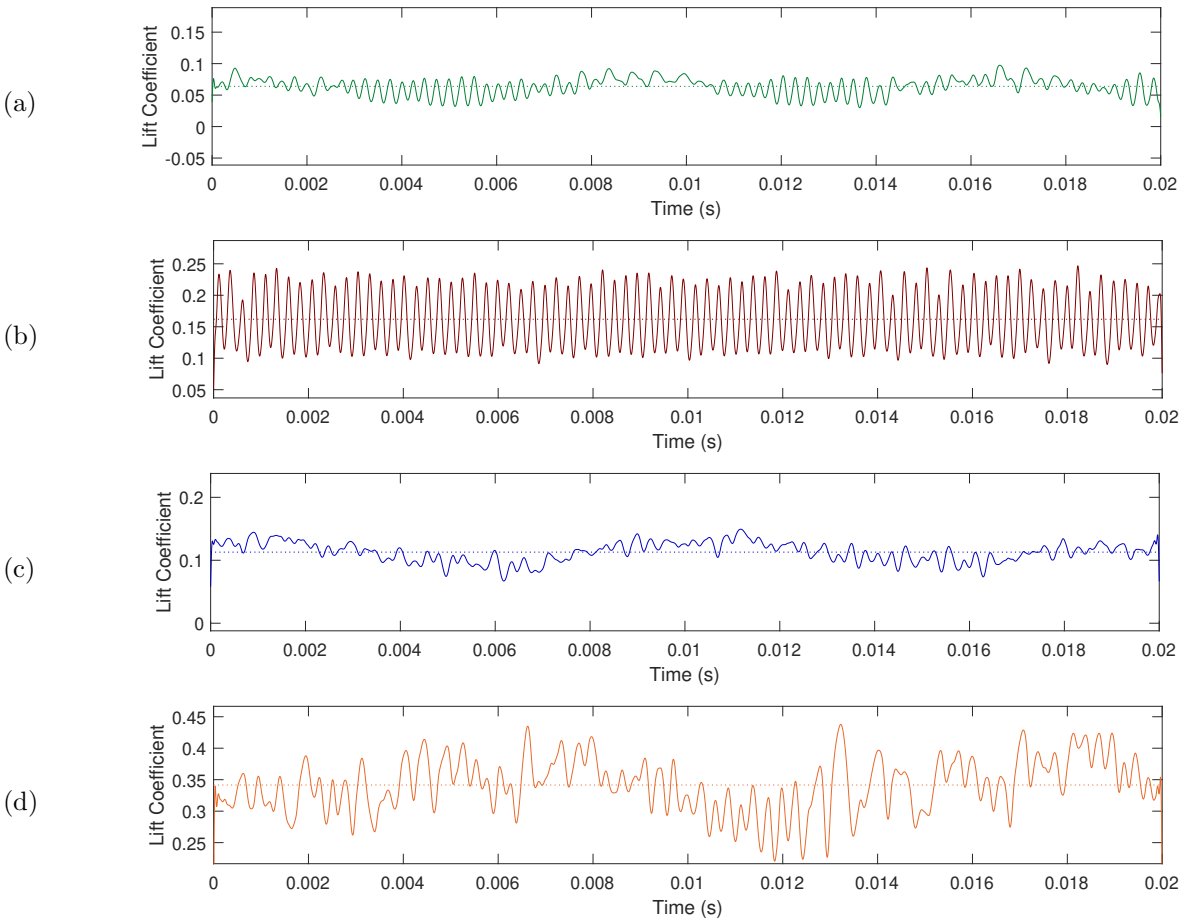

Figure 5.3: Case 3, 3a, 4 and 4a lift coefficient time histories for the final 20,000 time steps. Average values indicated by dotted line, vertical axis limits ± 0.125 the average value for each case.

The drag coefficient time histories for the four cases are shown in Figure 5.4 and show similar patterns to the lift coefficient time histories. The compressible cases show lower amplitudes than the corresponding incompressible cases. The fluctuations of Case 3a in Figure 5.4b show a less regular pattern when compared to the lift data, but is still the most regular out of the four cases. The data for both the lift and drag histories are taken from the same times in the simulation, so when looking at Case 3 (Figure 5.4a), it can be seen that the regular fluctuations in the drag history occur at the same time as the lift history. Also it can be concluded that the mechanism causing these fluctuations is decreasing the lift while simultaneously increasing the drag on the airfoil. The drag coefficient behaviour mirrors the behaviour in the lift coefficient time histories, and the following sections examine the velocity field and the wake behaviour to determine the flow differences causing these patterns.

(a)

(b)

(c)

(d)

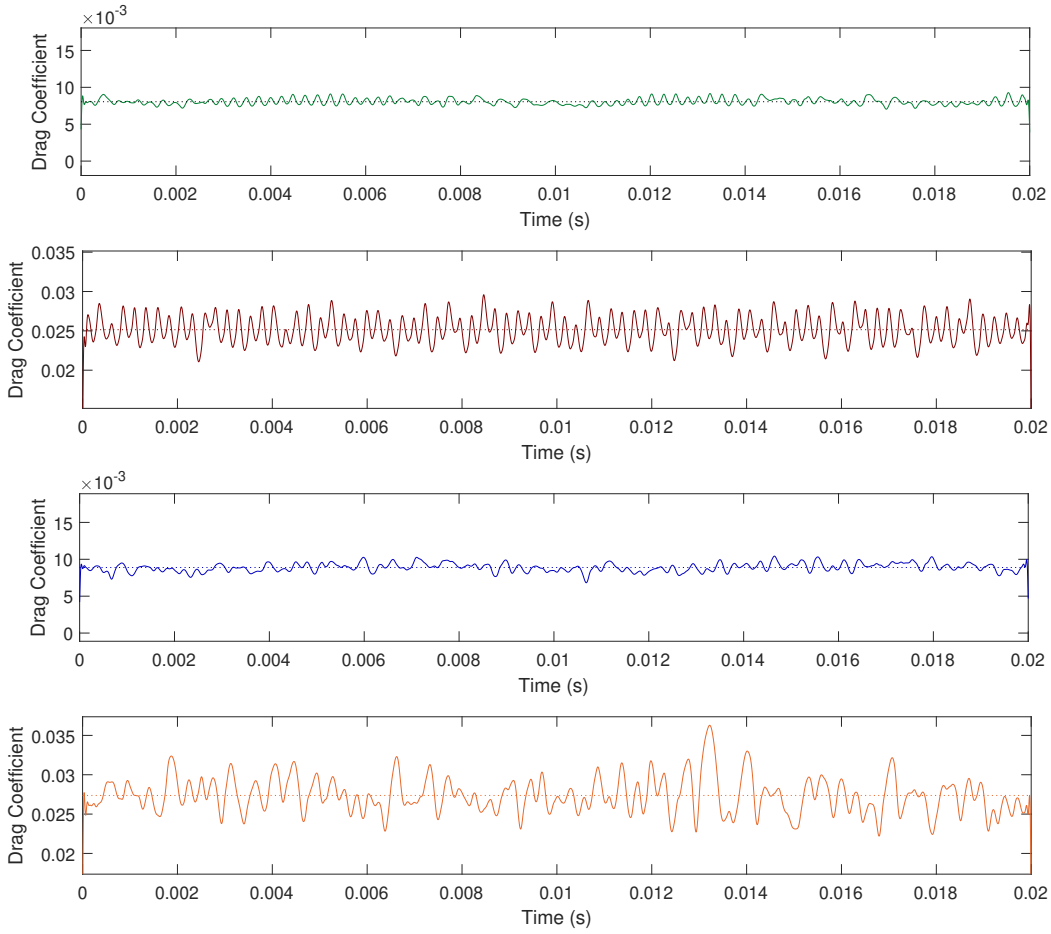

Figure 5.4: Case 3, 3a, 4 and 4a drag coefficient time histories for the final 20,000 time steps. Average values indicated by dotted line, vertical axis limits ± 0.01 the average value for each case.

5.1.2 Velocity Field Comparisons

The mean velocity field is a useful comparison tool for transient simulations since it shows the overall trend for the boundary layer and wake fluctuations. For this comparison, the velocity is broken down into X and Y components and then divided by the inlet velocity magnitude of $24.8m/s$ to create a non-dimensional result. Figure 5.5 shows the X-direction mean velocity fields and Figure 5.6 shows the Y-direction mean velocity fields for all four cases and compares them to experimental PIV data from Ghorbanishohrat at $Re = 42,500$ [2]. Overall, the X-velocity contours are very similar with differences appearing along the pressure side of the airfoil and in the trailing edge region of the suction side. For the pressure side, the velocity contours are very similar for each simulated AOA, but the 0° cases have overall a higher velocity than the 1° cases. When this is compared with the experimental results, all four cases have a slightly higher velocity than the PIV results, but still contain the same pattern. The TE region differs when considering the dark blue region of negative velocity, where Case 3 and 3a have a this region extending a little farther into the wake than Case 4 and 4a. All cases show this region with a stronger negative velocity than the experimental data, but the overall size and shape of the region is the same.

The Y-velocity data also is in good agreement, though there are larger differences between the cases than in the X-velocity data. The experimental Y velocity field shown in Figure 5.6f shows a consistent pattern of alternating low and high velocity regions in the wake, indicating that the vortices shed in the experimental case remain consistent with time. For all simulated cases, except for Case 3a, these vortices are less consistent with time and are therefore not visible in the averaged data. Case 3a (Figure 5.6c) shows the most agreement since it has the alternating velocity pattern in the wake and has almost identical contour locations with the exception of the yellow region of increased velocity on the pressure side. Case 3 and 3a look very similar except for the vortex pattern in the wake and Case 4 and 4a are also the same with some differences in the wake region of Case 4a. As with the X-velocity, there are general differences between the 0° and 1° simulated results, with an overall increase in Y-velocity occurring and also a decrease in the strength of the positive velocity regions at the TE and on the suction side of the airfoil near the TE. These differences in the trailing edge and wake behaviour could be seen in the C_P plot in Figure 5.1a and may also explain differences in the lift and drag coefficients between the compressible and incompressible simulations.

(a) X-Velocity Scale

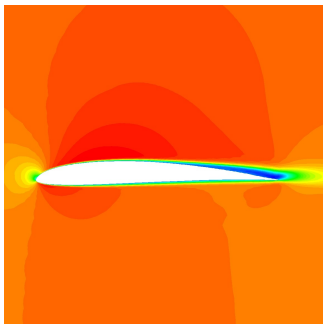

(b) Case 3 X-Velocity

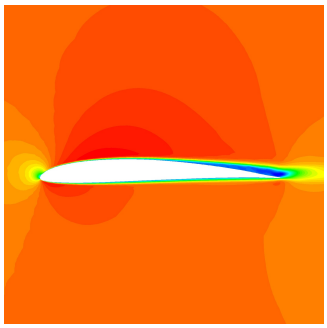

(c) Case 3a X-Velocity

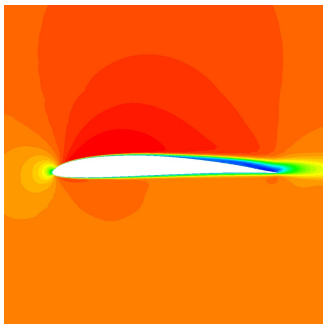

(d) Case 4 X-Velocity

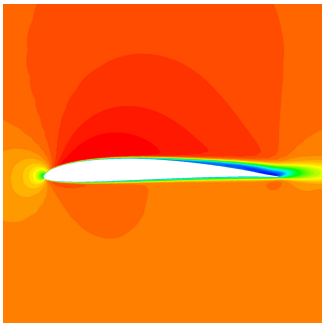

(e) Case 4a X-Velocity

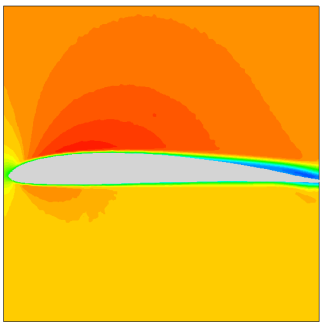

(f) Exp. X-Velocity [2]

Figure 5.5: Case 3, 3a, 4 and 4a mean X velocity compared with PIV results by Ghorbanishohrat [2]. Velocities are non-dimensionalized with the free stream velocity.

(a) Y-Velocity Scale

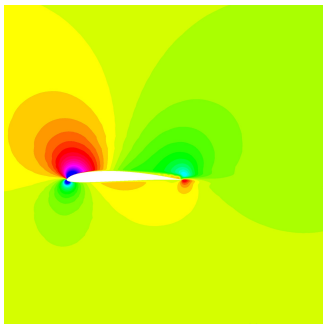

(b) Case 3 Y-Velocity

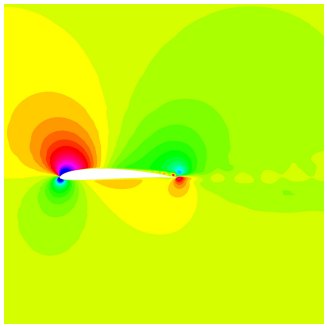

(c) Case 3a Y-Velocity

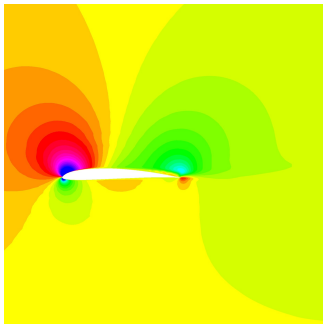

(d) Case 4 Y-Velocity

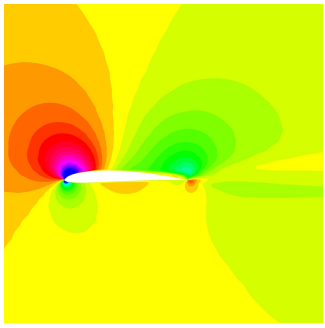

(e) Case 4a Y-Velocity

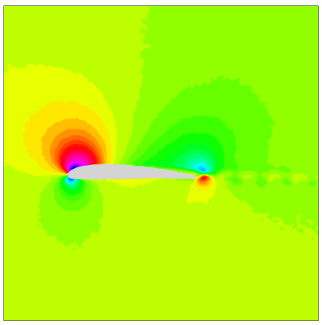

(f) Exp. Y-Velocity [2]

Figure 5.6: Case 3, 3a, 4 and 4a mean Y velocity compared with PIV results by Ghorbanishohrat [2]. Velocities are non-dimensionalized with the free stream velocity magnitude.

The mean data for the velocity fields shows that in general, the simulations have accurately predicted the velocity for the given flow conditions. There are no large differences between the four cases, so no conclusions can be drawn about the source of the differences of the lift and drag coefficients and their time histories. The transient wake behaviour of the four simulated cases is explored in the following section to further investigate the differences between the simulations.

5.1.3 Wake Behaviour

The behaviour of the wake of an airfoil is important for acoustic simulations since the majority of airfoil self noise mechanisms depend on the interaction of the boundary layer and the trailing edge of the airfoil. More specifically, changes in the boundary layer and wake behaviour can pinpoint which self noise mechanism is present in the flow. The low Re and low AOA here should result in a laminar boundary layer, and therefore the LBL-VS noise mechanism should generate tonal noise for the four cases. Before relating the wake behaviour to the noise generated by the airfoil, an in depth look at the wake behaviour is needed. Due to the large amount of transient data collected during the simulations, it is possible to analyze the transient behaviour of the wake and relate these behaviours back to the differences seen in the lift and drag coefficients.

The first analysis of the wake is a visual comparison of the vorticity in the wake for the four cases. For all cases, an iso-surface is generated in Fluent where the vorticity magnitude is $10,000$ $[1/s]$ and then coloured with a contour of Y velocity limited to the range of ± 5 m/s. This comparison is taken from different time steps in the simulations, and the times for Case 3 and 3a are shown in Figure 5.7a. The wake behaviour for Case 3a, shown in Figure 5.7b, shows an undulating pattern indicating that there are vortices being shed from the trailing edge of the airfoil. This image is taken from the last simulated time step, but the wake behaviour is consistent throughout the simulation. It is most likely that the fluctuations seen in the lift and drag time histories are due to the vortices being continuously shed and altering the pressure distribution near the trailing edge of the airfoil. Another important note is that there is no spanwise variation in the wake and therefore the wake behaviour is 2D. This consistency with time and across the span of the airfoil also explains why the amplitude of the lift and drag coefficients are higher than the other cases, because pressure changes on the surface apply across the entire span and have a cumulative effect.

The wake behaviour for Case 3 is much different from Case 3a, even though they are simulating the same AOA. Figure 5.7c shows a similar behaviour to the 2D wake found in Case 3a, but Figure 5.7d shows 3D wake behaviour that occurs at a different time step in the simulation. When comparing the lift time histories in Figure 5.7a, the 2D wake behaviour occurs in the regions that experience more regular fluctuations, which is the same regions with that most closely resembles the fluctuations in the lift coefficient Case 3a. This indicates that the regular lift and drag coefficient fluctuations occur when the airfoil is shedding vortices at a regular frequency in a 2D wake. The 2D behaviour in Case 3 does exhibit some inconsistencies across the span beginning near the trailing edge of the airfoil, which may explain why the amplitude for the lift coefficient is not as high

as for Case 3a. When the Case 3 simulation is between the 2D wake regions, the wake behaviour transitions to 3D, as seen in Figure 5.7d. Since the wake is behaving differently across the span of the airfoil, the vortices that are shed do not have a combined impact on the lift properties of the airfoil and therefore do not create a regular pattern in the lift and drag coefficient time histories. For the 3D wake, the beginning of the transition from 2D to 3D behaviour occurs further upstream from the trailing edge, and therefore the transition point must be shifting upstream and downstream during the changes in lift coefficient behaviour.

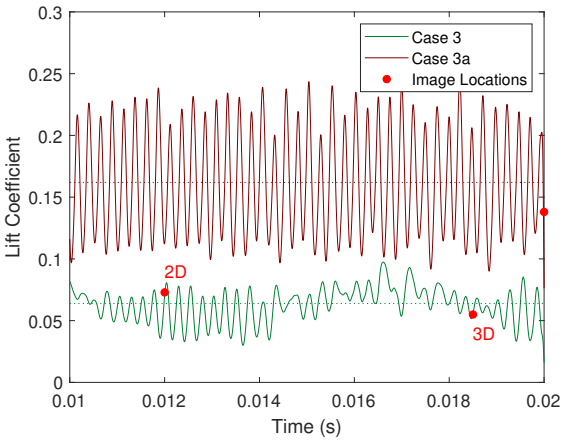

(a) Image Locations

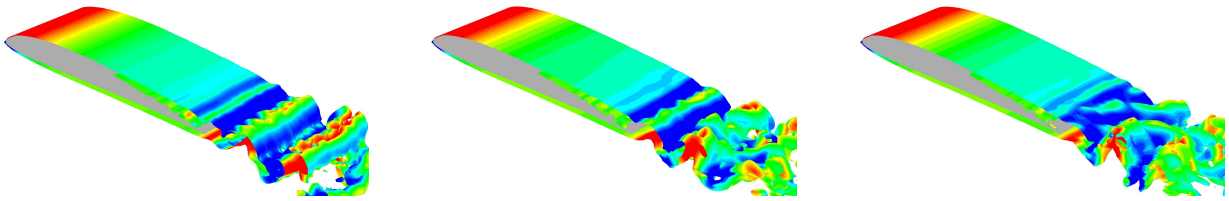

(b) Case 3a (c) Case 3 - 2D (d) Case 3 - 3D

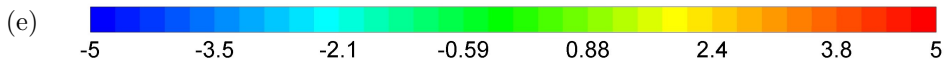

Figure 5.7: Case 3 and 3a iso-surface of Vorticity Magnitude = 10000 $1/s$ coloured with Y-Velocity from -5 to $+5$ m/s

The wake comparisons for Case 4 and 4a are taken from the three time steps indicated in Figure 5.8a. Case 4a has consistent 3D wake behaviour, and the transition from a 2D to 3D wake can be seen further upstream than in Case 3. Since the AOA is a degree higher,

it is expected that any patterns in the boundary layer behaviour shift from the trailing edge toward the leading edge. As with the 3D wake in Case 3, the inconsistent spanwise behaviour for Case 4a results in a lift and drag coefficient time history with no discernable pattern. Like Case 3, Case 4 changes between having a 2D wake and a 3D wake, but unlike Case 3, the majority of the time it has a 3D wake as opposed to a 2D wake. Figure 5.8c shows the 2D wake behaviour for Case 4, which occurs when the lift coefficient is below the average value. When compared to Case 3 and 3a, the 2D wake is not as well defined and appears to be on the verge of transition to a 3D wake. This absence of a well defined 2D wake explains why the lift coefficient time history for Case 4 does not have a regularly fluctuating region like it does in Case 3. The final image of the vorticity iso-surface is for the 3D wake in Case 4, which closely resembles the behaviour of Case 4a.

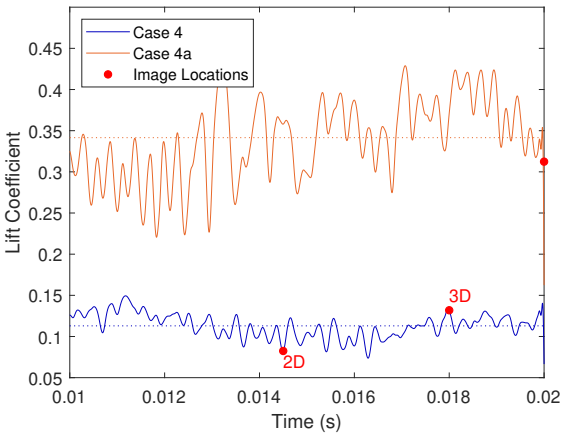

(a) Image Locations

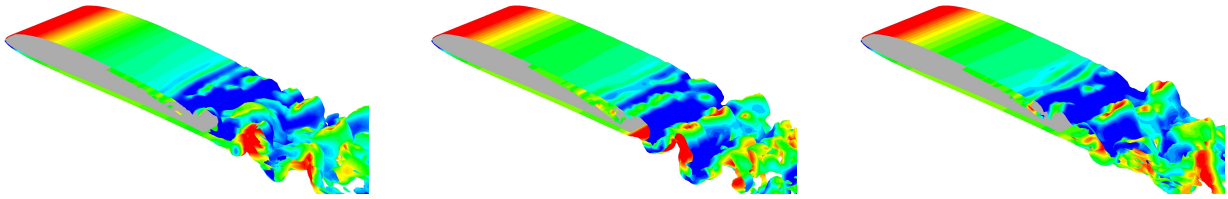

(b) Case 4a (c) Case 4 - 2D (d) Case 4 - 3D

(e)

Figure 5.8: Case 4 and 4a iso-surface of Vorticity Magnitude = 10000 $1/s$ coloured with Y-Velocity from -5 to $+5$ m/s

The following sets of figures examine the instantaneous Y velocity contour of the mid-plane of the airfoil span, with the range limited to $\pm 5\ m/s$. These are selected for the same time steps as the vorticity magnitude iso-surface images above. The contour plot for Case 3a is shown in Figure 5.9b and has very clearly defined pockets of positive and negative velocity that persist well downstream of the airfoil. In comparison, Figure 5.9c shows the 2D wake behaviour for Case 3, which is not as well defined but still has alternating areas of positive and negative velocity. Since Case 3 is changing between 2D and 3D wake behaviour, it is expected that the 2D behaviour will not be as well defined as a simulation that maintains its 2D behaviour. The 3D behaviour for Case 3 definitely does not show an alternating pattern, and does not have strong positive or negative velocities propagate very far downstream.

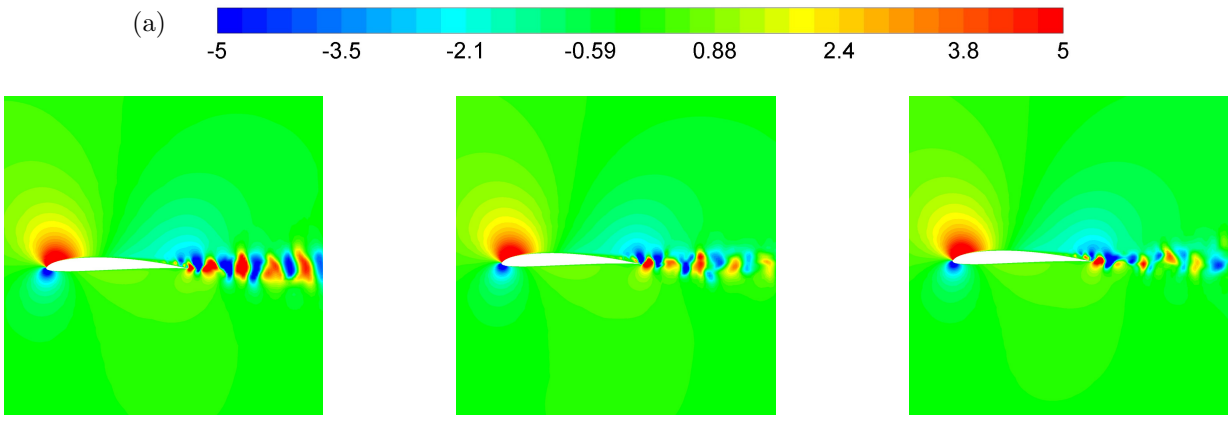

(b) Case 3a (c) Case 3 - 2D (d) Case 3 - 3D

Figure 5.9: Case 3 and 3a instantaneous Y-velocity limited from -5 to $+5\ m/s$

The Case 4a wake has fully transitioned to 3D behaviour and interestingly the Y velocity contour shown in Figure 5.10b has disorganized yet strong velocity fluctuations in the wake. When compared to the 3D wake in Case 3, the velocity fluctuations propagate much farther downstream. This may be due to differences between compressible and incompressible simulations, which were run using different boundary offsets for the domain geometry. Figure 5.10c shows the 2D wake behaviour of Case 4, and even though the iso-surface image showed a wake beginning the transition to 3D behaviour, the velocity contour shows fluctuations closest to the strong 2D behaviour seen in Case 3a. On the other hand, the 3D wake behaviour of Case 4, shown in Figure 5.10d, has very small areas of positive and negative velocity, indicating that there is a lot of mixing occuring to disrupt any fluctuating patterns in the wake.

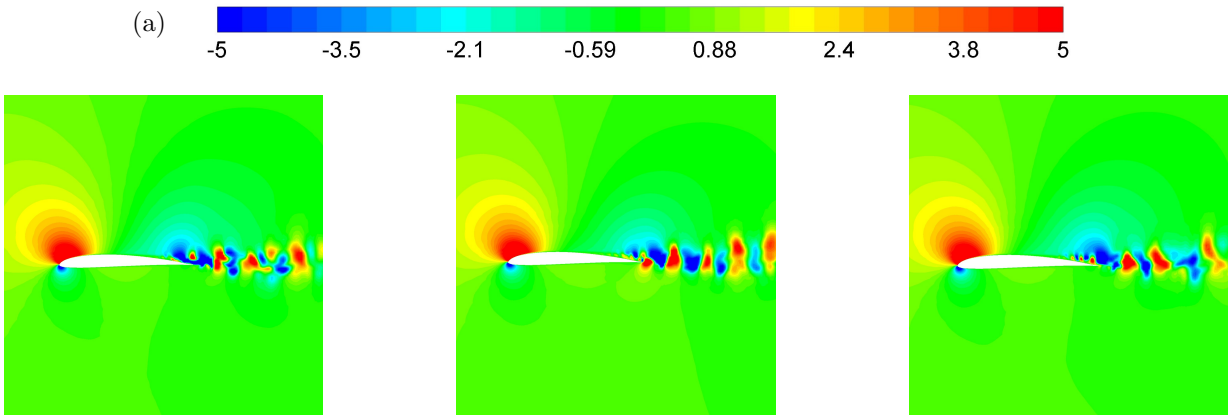

(b) Case 4a (c) Case 4 - 2D (d) Case 4 - 3D

Figure 5.10: Case 4 and 4a instantaneous Y-velocity limited from -5 to $+5$ m/s

The wake for Case 3, 3a, 4 and 4a show large differences in behaviour which can be related to the patterns seen in the lift and drag coefficient time histories. These differences were not visible in the averaged data presented in the previous section, and uncover interesting differences between compressible and incompressible simulations. The compressible simulations for both 0 deg and 1 deg AOA alternate between having a regularly oscillating 2D wake and an irregular 3D wake, with the 0 deg AOA staying largely 2D and 1 deg AOA staying mostly 3D. The incompressible simulations have wake behaviour that stays consistent throughout the entire simulation, and for each AOA, the incompressible simulation has the same wake behaviour as the dominant behaviour in the compressible solution. These conclusions should be taken with caution, since there are small differences in the mesh sizing near the airfoil that may impact the ability to resolve sensitive boundary layer behaviours and feedback mechanisms. But there is also a possibility that the feedback mechanisms that cause the alternating behaviour in the compressible simulations are triggered by changes in the density due to noise generation at the trailing edge.

5.1.4 Suction Side Laminar Separation Bubble

The SD 7037 airfoil generates a LSB, which occurs for flow at low Reynolds numbers and at low AOAs. The behaviour of this bubble was the focus of the research by Ghorbanishohrat, which included surface oil flow visualization in addition to PIV analysis [48]. Two sets of oil visualization were gathered at a similar Reynolds number to the simulations at AOAs of 1° and 2°, which are shown as white oil on a dark airfoil in Figures 5.11b and 5.11f for

$Re = 40,000$, and Figures 5.11e and 5.11i for $Re = 41,700$. Oil flow visualization was not collected for 0°, but Section 5.1.1 discusses the similarity between the simulated 0° AOA case and the 1° experimental C_p (Figure 5.1a) so the 1° experimental data should provide a useful comparison to the simulated cases. In addition, the $Re = 40,000$ images are at a lower Reynolds number than the simulated case, and therefore give an approximation of a lower AOA at the simulated Re.

The simulated cases are represented with a mean X-direction shear stress contour on the surface of the airfoil, since low shear stress values caused by slower air flow results in oil accumulation and regions of undisturbed oil. The simulated results are shown with the oil flow visualization images in Figure 5.11, with the shear stress scale shown in Figure 5.11a. The simulated results each show a large blue region on the downstream half of the airfoil, in which the shear stress is approximately zero or less than zero. This area corresponds to the white areas on the oil flow images, which is where the oil is undisturbed due to the presence of the LSB. Since the exact shear stress to cause oil movement is unknown, pinpointing the start and end of the bubble in this visual comparison is difficult but can be generally approximated when the shear stress increases above $0Pa$. Comparisons between the simulated results and oil flow images are based on the approximate location of separation, oil accumulation, and reattachment of the LSB. The separation location is where the shear stress drops below zero and the reattachment is when it is increases back above zero. The oil accumulation line is an early sign of reattachment and occurs where the negative shear stress is the largest, since the shear stress is high enough to prevent any oil within the LSB from moving downstream and results in a slight pooling of the oil [2]. The locations for separation and the oil accumulation line are shown on the oil flow images with horizontal red lines, and only the separation location is indicated on the simulated results.

Case 3a, shown in Figure 5.11c, shows separation location of the LSB just past half of the chord length and has increased shear at the TE indicating the LSB shows early signs of reattachment at the trailing edge. This shows similar reattachment behaviour to the $Re = 40,000$, 1° AOA oil flow image in Figure 5.11b, where there is a thin black line at the TE defining the oil accumulation line. However, this oil accumulation behaviour may not be caused by the bubble reattachment, but may be due to upstream effects of the vortices shed from the TE of the airfoil. The positive Y-velocity at the TE can be seen in the mean y velocity field of Figure 5.6c and in the instantaneous image in Figure 5.9b. Case 3 and Case 3a have almost identical separation locations, which line up with the 1° AOA location for $Re = 40,000$. Case 3, even though it is a 0° case, has a similar oil accumulation location to the $Re = 41,700$, 1° AOA oil flow image in Figure 5.11e. This agrees with the C_p results from the beginning of this chapter, which also uses averaged data. When considering the

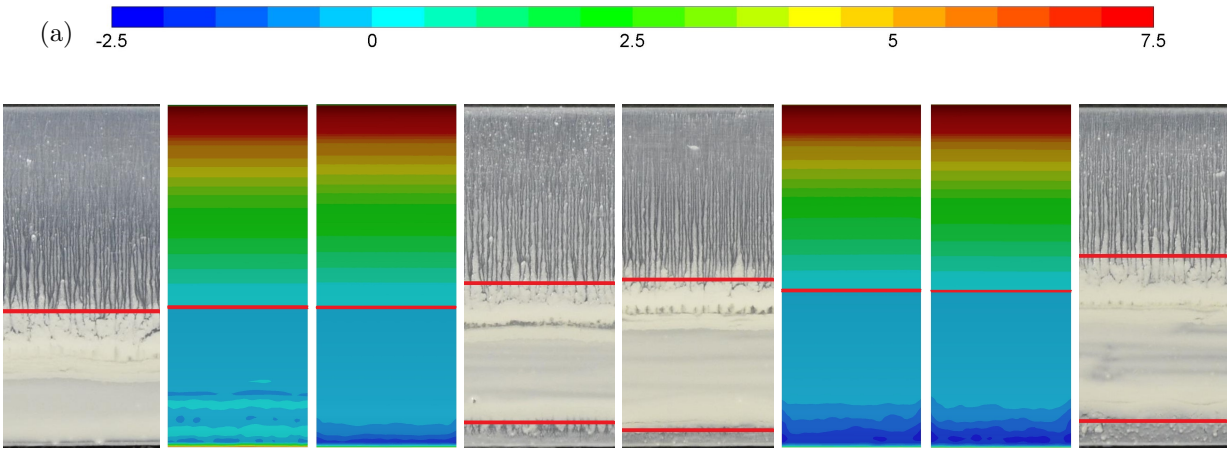

(b) 1° AOA $Re = 40,000$ (c) Case 3a (d) Case 3 (e) 1° AOA $Re = 41,700$ (f) 2° AOA $Re = 40,000$ (g) Case 4 (h) Case 4a (i) 2° AOA $Re = 41,700$

Figure 5.11: Case 3, 3a, 4 and 4a mean X shear stress from -2.5 to 7.5 Pa compared with oil flow results by Ghorbanishohrat [48]. Flow direction top to bottom. Red lines indicate LSB separation are reattachment locations, image (b) has no reattachment line.

alternating 2D and 3D wake behaviour of this case, it can be assumed that the shear stress behaviour in Case 3 is averaged between the pattern shown in Case 3a (2D wake) and the behaviour in Case 4a (3D wake), which gives the impression that the airfoil is at a slightly higher AOA. Case 4 and 4a, Figures 5.11g and 5.11h, show the same behaviour, with the separation point for the LSB advancing upstream from the 0° AOA simulations, as expected. The oil accumulation location for Case 4 and 4a appears to extend further upstream than any of the oil flow images, but the exact negative shear stress required for oil accumulation is unknown. A closer look at the exact LSB behaviour is conducted below with the examination of the simulated skin friction coefficient. Overall, the location and size of the LSB agrees well with experiments conducted by Ghorbanishohrat at a similar Re.

The skin friction coefficient on the surface of the airfoil is calculated using the X-direction shear stress and even though the coefficient has no associated direction, the negative values are used to indicate where the shear stress is in the upstream direction. Figure 5.12a shows the calculated coefficient along the entire chord length of the airfoil, and Figure 5.12b highlights the back half of the airfoil to get a closer look at the LSB behaviour. As seen before in the C_p plot, the simulations conducted at the same AOA result in very similar overall trends, with some differences near the TE. The separation point for Case 3

and 3a is just before $x/c = 0.6$ and for Case 4 and 4a it is just before $x/c = 0.55$, which has good agreement with the separation lines in Figure 5.11. The oil accumulation location for each case is quite clear, with Case 4 and 4a being from $0.96 < x/c < 0.98$, Case 3 and 3a being at $x/c = 0.98$. When comparing these results with the oil flow images, the oil accumulation lines more closely align with where the skin friction coefficient increases to zero before dropping steeply down to the simulation-predicted oil accumulation location. Figure 5.12b clearly shows how reattachment occurs right at the trailing edge, with the earliest reattachment by Case 3a at $x/c = 0.985$. Since Case 3a should be the least likely to reattach (i.e. fully 2D wake), the reattachment is likely caused by interference of the vortices from the pressure side as mentioned above.

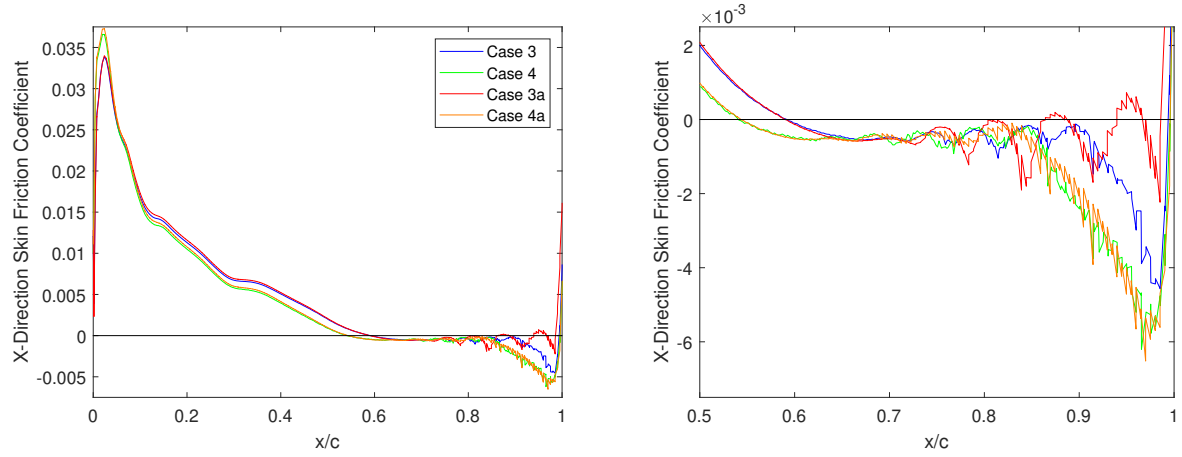

(a) Full Suction Side

(b) Trailing Edge

Figure 5.12: Case 3, 3a, 4 and 4a X-direction skin friction coefficient

The final tool for understanding the LSB behaviour is an analysis of the shape factor for the boundary layer. The key piece of information from the shape factors of the simulated cases is the location of the peak, which indicates the transition of the boundary layer from laminar to turbulent. A LSB is only fully reattached if the boundary layer has transitioned to turbulence, and this transition is also the source of 3D behaviour in the wake. The results from the simulated cases are broken down into 2D and 3D behaviour at the same time steps used in Section 5.1.3 and shown in one plot (Figure 5.13). It is clear that all cases have just approached the transition peak at the trailing edge of the airfoil, meaning that they cannot be fully reattached. This means the reattachment point indicated in the skin friction coefficient plot (Figure 5.12b) is a result of the mixing occurring when the suction side and pressure side boundary layers meet. This is likely the cause of the 3D wake

behavior downstream of the TE, since the suction side boundary layer does not transition soon enough to be the cause. An interesting trend in the shape factor plot is that the peak height is more dependent on the downstream wake behaviour (2D or 3D) than the angle of attack. It can be concluded that the 2D and 3D behaviour is not caused by the boundary layer transition, therefore there is still an unknown factor involved in the alternating 2D and 3D behaviour in the compressible cases.

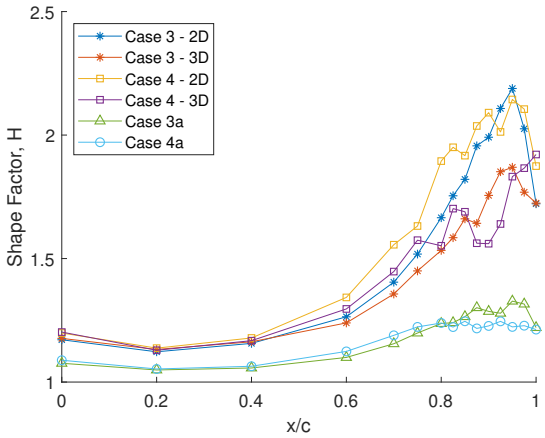

Figure 5.13: Case 3, 3a, 4 and 4a shape factor

The boundary layer and LSB analysis brings up an interesting point of discussion: what is the cause of the alternating 2D and 3D wake behaviour? One possibility is that this change occurs in experiments, but since the cycle is very short ($0.008s$) the PIV images do not capture this change. This might be the case, but in the simulations, the switch between 2D and 3D resulted in a less consistent 2D vortex shedding than it does in the case that it remains fully 2D. The PIV images exhibit this more regular 2D behaviour so it is more likely that the alternating 2D and 3D behaviour is not present in experiments. Another consideration is that this behaviour is only present in the compressible solutions, which allows density fluctuations in a situation that would largely be considered incompressible. The introduction of variable density may be triggering this behaviour, especially considering that the low AOA cases are meant to produce a sharp tonal noise that would involve the propagation of pressure waves that cause radial compression and expansion of the air density in the flow. These acoustic driven pressure and density fluctuations originate at the trailing edge of the airfoil, which is where the wake transitions from 2D to 3D behaviour. This is similar to the density caused feedback loop proposed by Fink [9], but in the simulations, this feedback could be sufficient to initiate the boundary layer transition

further upstream. Taking Case 3 as an example, the 2D wake produces regularly shed vortices that activate the LBL-VS airfoil self-noise mechanism, and the tonal noise produced by that causes the wake to transition to 3D. This has an upstream effect as well, changing the behaviour at the TE of the airfoil which stops the tonal noise. Then in the absence of tonal noise, the TE behaviour returns to the 2D behaviour and starts the cycle over again. The final possibility is that the combination of mesh sizing and simulation settings used is unintentionally triggering this change in wake behaviour. This could be determined by performing a grid independence study and testing alternative solver settings. Due to time restrictions, this was not completed for this research and instead the results were validated using the experimental PIV and oil flow data above.

5.2 Acoustic Results

This section analyses the acoustic results for the four simulated cases of the SD 7037 airfoil and compares them with the experimental data collected by Tam [35]. The previous section explored the differences in the flow behaviour for the two different AOAs and the impact of using an incompressible or compressible solution. In this section, the effect of these flow behaviours on the acoustic behaviour of the airfoil is determined and conclusions are drawn about the ability of the simulation to predict the acoustic behaviour in the given conditions.

5.2.1 Acoustic Signal Comparison

The acoustic data gathered from the simulation is in the form of an acoustic pressure signal measured by the 15 receivers (Figure 4.4). The acoustic pressure signal for each receiver is a result of the application of the FW-H acoustic analogy to the pressure distribution on the surface of the airfoil. The signal from each microphone is identical, with slight phase shifts as a result of the extra distance travelled between the airfoil and the receiver. Figure 5.14, shows the signal for receiver 8 which is aligned with the mid-plane of the airfoil span (i.e. directly below the airfoil). The signals have had a bandpass filter applied to clearly show the frequencies ranging between 1 and $10kHz$. These signals are shown for the final $0.02s$ of the measured signal, which is also the same times used for the lift and drag coefficient histories in Figures 5.3 and 5.4.

The acoustic signal for each case shows almost identical behaviour to its lift and drag history, especially for Case 3 and 3a. Case 3, shown in Figure 5.14a, has the same sections of

regular frequency and high amplitude separated by sections of lower amplitude oscillations of varying frequencies. Figure 5.14b shows that the acoustic pressure fluctuations remain at a high amplitude and consistent frequency, which is also the same as the lift and drag behaviour. From these two 0° AOA cases, it can be shown that the lift coefficient time history is a good indicator of the acoustic signal behaviour. In Figure 5.7a, it was shown that the regular frequency fluctuations of the lift coefficient correspond to 2D behaviour in the wake, and since these fluctuations are present in the acoustic signal, it can be concluded that the 2D wake is responsible for the high amplitude fluctuations in the acoustic signal. It should be noted that even though the lift coefficient amplitudes between the compressible and incompressible 0° cases are different, the acoustic pressure amplitude is relatively the same. This holds true for the 1° AOA cases, where the lift amplitude for Case 4a is much higher than for Case 4, yet the acoustic signal in Figure 5.14c and 5.14d is the same amplitude. There is no dominant frequency present in the acoustic signal for Case 4 and 4a, which follows similar behaviour to the lift coefficient. This is also true for the irregular regions found in the Case 3 signal. The irregular frequencies can be tied back to the spanwise variation in the flow found in the 3D wake behaviour of Case 4 and 4a (Figure 5.8a).

The microphone measurements made by Tam are presented as a signal of voltage versus time for AOAs of 0° to 3° in Figures 5.15a-5.15d [35]. As with the simulation results, a bandpass filter has been applied with the range of 1 and $10kHz$ to highlight the key frequencies in the signal. Since the microphone data is presented as voltage, a direct comparison of the signal amplitudes is not possible but a useful comparison of signal behaviour is possible. The experimental voltage signals show a very low amplitude and inconsistent frequency fluctuation at 0° which then jumps to a high amplitude and consistent frequency at 1°. The 1° experimental signal most closely resembles the acoustic pressure signal of Case 3a, and the 0° experimental signal does not appear to match the patterns in Case 3 or 3a. The experimental signals for 2° and 3° show a gradual decrease in amplitude while maintaining a relatively consistent frequency. The frequency and amplitude patterns in Case 4 and 4a seem to match the closest with those in the 3° experimental signal. Interestingly, the none of the recorded signals have the cyclical behaviour that is found in the results for Case 3 and 4.

(a)

(b)

(c)

(d)

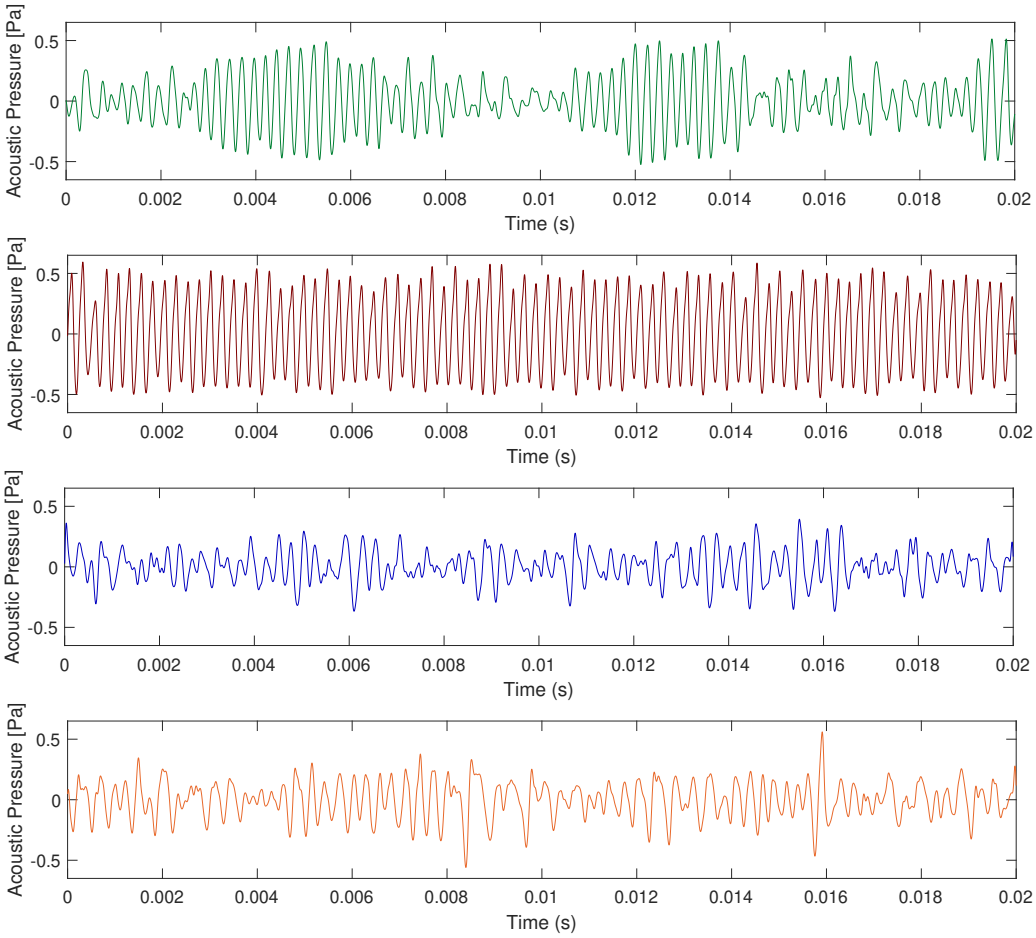

Figure 5.14: Case 3, 3a, 4 and 4a acoustic pressure signal (Pa) at the receiver for the final 20,000 time steps. (a) Case 3 (b) Case 3a (c) Case 4 and (d) Case 4a.

(a)

(b)

(c)

(d)

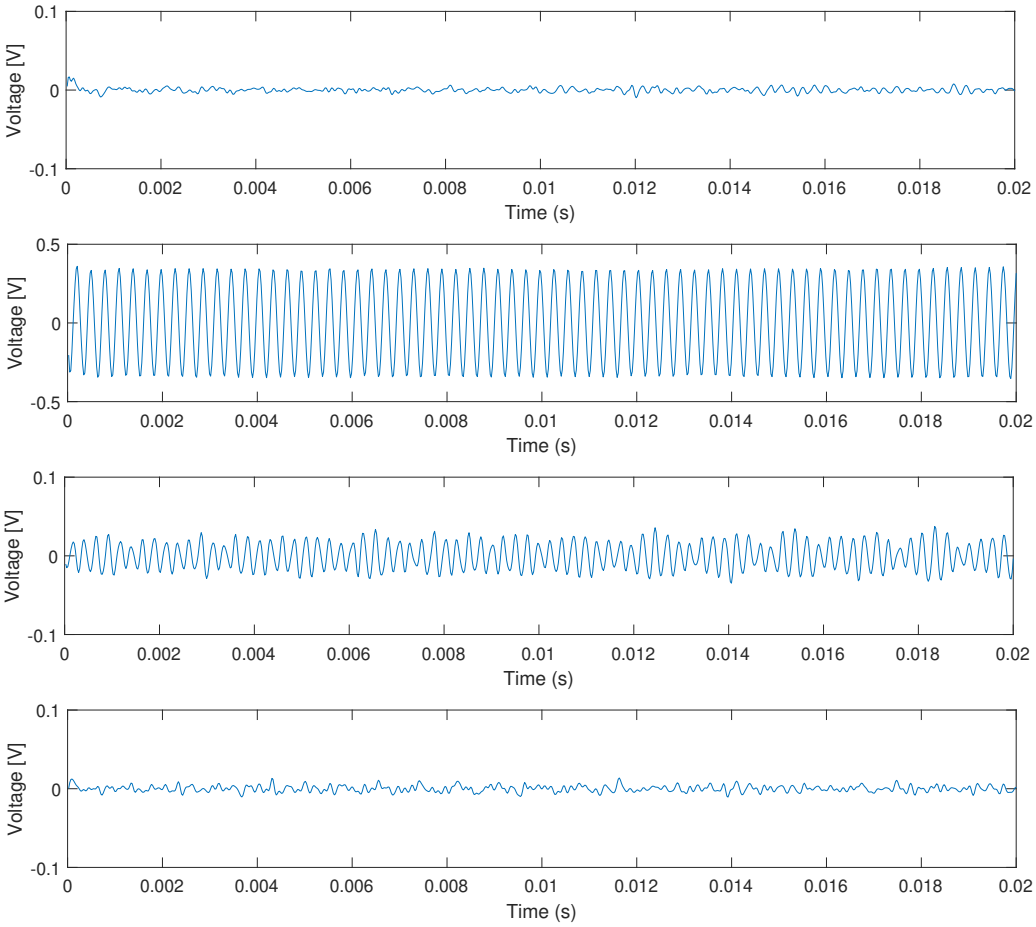

Figure 5.15: 0°, 1°, 2° and 3° AOA voltage signal (V) for 0.02s measured by Tam [35]. (a) 0° AOA (b) 1° AOA (c) 1° AOA and (d) 1° AOA.

5.2.2 FFT and 1/3 Octave Band Results

The acoustic signals for all 15 receiver locations were processed using the FFT algorithm in Matlab (see Appendix A), and the acoustic pressure for each frequency band was then converted to SPL. For each frequency band, the SPL for each receiver was added together to get the total SPL for the airfoil span equivalent to the experimental span. The results for each case are presented in Figure 5.16 and 5.18, and compared against the acoustic spectra measured by Tam for the same AOA [35]. The spectra results for Tam's experiments were produced with an ensemble average of the FFT results, which were performed on signal segments $1s$ in length. The simulated signals were processed for a length of $0.0405s$, and resulted in wider frequency bins in the narrowband spectra and prevents a direct comparison of SPL. To counteract this, the experimental bins were added together to result in the same bin widths as the simulated results. These plots highlight the two frequencies in the experiments where sharp peaks occurred, indicating tonal noise. These were measured at $3.4kHz$ and $4.1kHz$, and are indicated on the plots with vertical dotted lines.

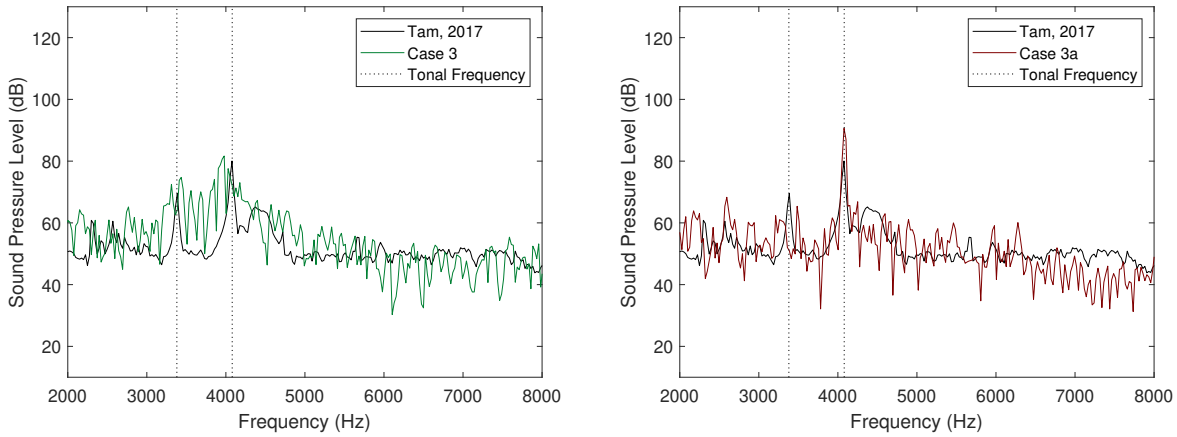

(a) Case 3 (b) Case 3a

Figure 5.16: Case 3, 3a acoustic spectra. Results plotted against 0° AOA experimental data from Tam [35]

The simulated and experimental 0° results are shown in Figure 5.16, with the compressible Case 3 data in Figure 5.16a and the incompressible Case 3a data in Figure 5.16b. Overall, both cases match the trend in the acoustic spectra with the simulated data having a coarser appearance with sharp peaks and troughs. This is a result of the short simulated

signal time which led to an inability to average the FFT results to gain smoother peaks. A longer acoustic pressure signal would produce narrower frequency bin widths as well as allow for splitting of the signal into smaller segments that could be processed separately and averaged. With this coarser data, it is still possible to analyze the trend in the data around the locations of the experimental tones. First, Case 3a has a peak of $90dB$ at the $4.1kHz$ tone which extends well above the broadband noise and clearly defines a simulated tone at this frequency. However, the $3.4kHz$ tone does not appear to be simulated since any peaks near that frequency do not extend above the average fluctuations in the rest of the spectra. The strong tone at $4.1kHz$ is the dominant frequency in Case 3a and is the result of the consistent high amplitude oscillations in the acoustic signal (Figure 5.14b), which has been related to the 2D wake behaviour of this simulation. Now for Case 3, there is a consistent pattern of increased SPL around both the $3.4kHz$ and $4.1kHz$ tones in the experimental results. When looking at its acoustic signal, the high amplitude portions that appear as a result of the 2D wake are dominated by the $4.1kHz$ frequency oscillations. The lower amplitude oscillations that occur during the 3D wake are largely dominated by a $2kHz$ frequency. The location of the $3.4kHz$ tonal behaviour occurs in the transition between the 2D and 3D wake behaviour. The frequency behaviour of the signal is shown in Figure 5.17, with a $3.4kHz$ signal overlaid with the region associated with the 3D to 2D wake transition, and the $4.1kHz$ signal aligned with the acoustic pressure oscillations in the 2D wake region. This plot serves as a visual representation of the regions associated with the tonal peaks in the narrowband acoustic spectra.

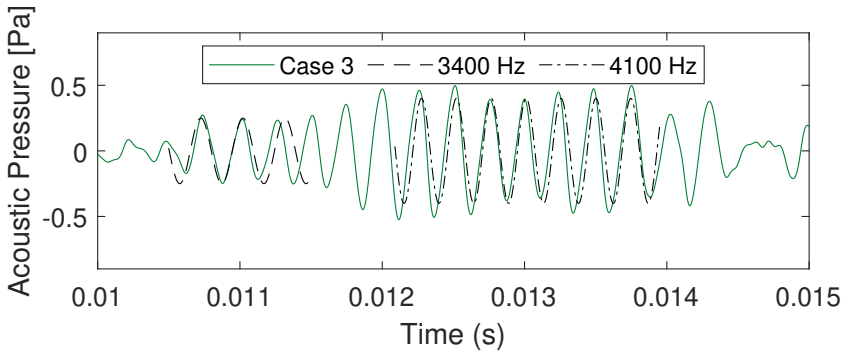

Figure 5.17: Case 3 location of tonal frequencies in the acoustic signal

The 1° acoustic spectra results are shown in Figure 5.18 and compared against the experimental data. Both the compressible and incompressible cases show similar trends which largely agree with the experimental data. In the higher frequencies, both cases appear to dip about $10dB$ below the trend in Tam's data. The 1° AOA was shown to

have the largest tonal noise for the experiments, reaching a peak of $120dB$ for the $3.4kHz$ tone. Case 4 and 4a do not simulate this tone, which is not surprising when looking at the irregularity of the acoustic signal in comparison with that of Case 3a. The general trend does increase to a maximum value around $3.4kHz$, but fails to produce the sharp peak. From the analysis of Case 3 and 3a, it was proposed that the $3.4kHz$ is a result of the transition between the 2D and 3D wake behaviour. The wake analysis in Section 5.1.3 showed that Case 4a remained 3D for the entirety of the simulation, and Case 4 spent the majority of time with 3D wake behaviour and cyclically transitioned to partially 2D behaviour. This would explain why the tone is not produced, since it is likely that a strong $3.4kHz$ tone is a result of the wake remaining in a transitional state between 2D and 3D behaviour.

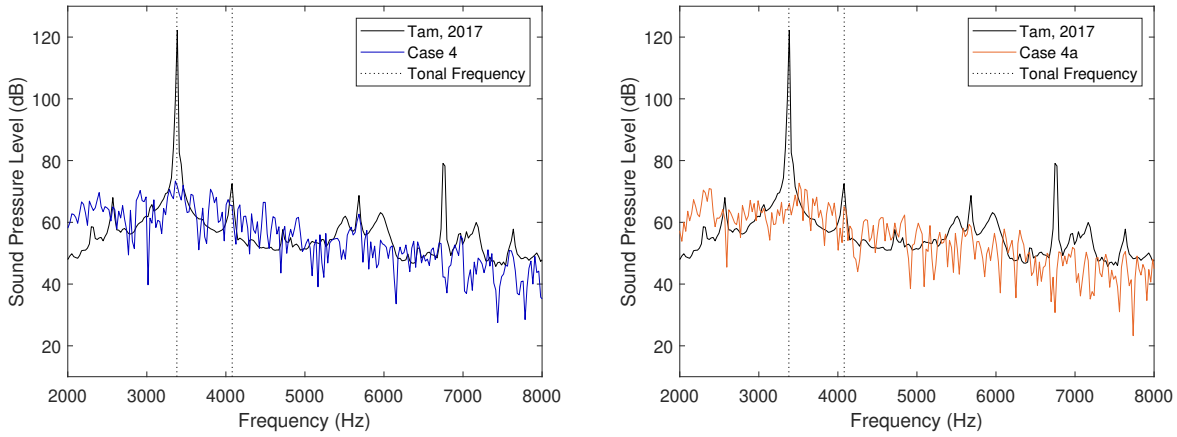

(a) Case 4

(b) Case 4a

Figure 5.18: Case 4 and 4a acoustic spectra. Results plotted against 1° AOA experimental data from Tam [35]

A common method of comparison of acoustic results is the use of 1/3 octave bands, since it combines the frequency bins from the narrowband spectra in a standard way while also accounting for the increasing frequency ranges for each successive octave. Figure 5.19a compares the 0° AOA experimental and simulated results, which shows accurate prediction of the SPL. As mentioned previously, the averaging of multiple signal segments in the experimental data resulted in a much smoother acoustic spectra and well defined tonal peaks. The wider peaks for Case 3 and 3a result in an overprediction of the SPL in the tonal regions of the 1/3 octave band data. The trend in the 1/3 octave band for these cases shows an accurate prediction of the acoustic behaviour of the SD 7037 airfoil at 0°. The 1°

1/3 octave band comparison is shown in Figure 5.19b and gives a good approximation of the broadband noise produced in the experiments. The inability to simulate the $3.4kHz$ tone is shown clearly in this plot, in addition to the peak for the second harmonic of the tone at $6.8kHz$, is what causes the large deviation from the experimental results. Again, the tones are not present in the 1° simulated results because the 3D wake behaviour does not have sufficient periods of time with 2D behaviour to generate the tonal noise in the acoustic spectra.

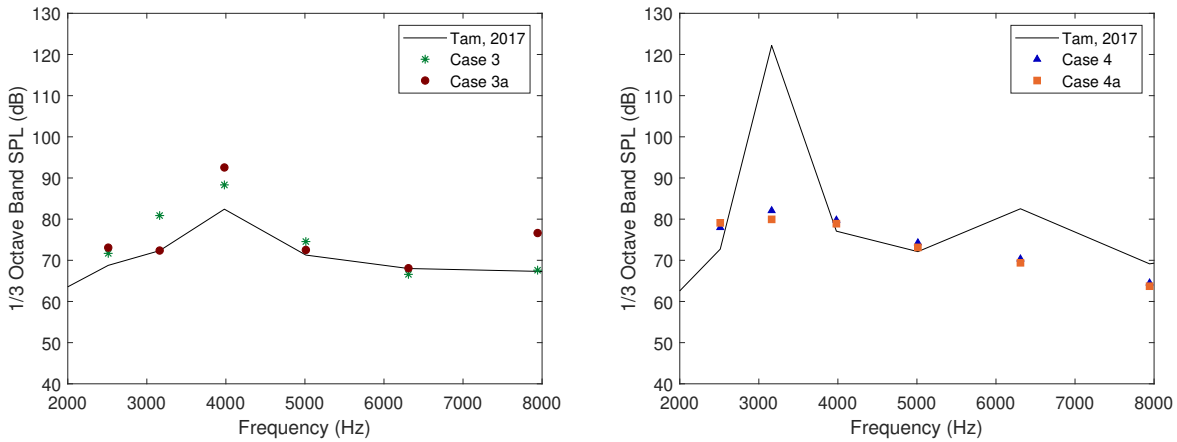

(a) 0° AOA (b) 1° AOA

Figure 5.19: SD-7037 one third octave band results for Case 3, 3a, 4 and 4a. Results plotted against experimental data from Tam [35]

The cause of the transition between 2D and 3D behaviour in the compressible simulations was discussed at the end of Section 5.1.4, with the major possibilities being instabilities caused by the density changes created by tonal noise generation, or the simulation and solver settings. It is clear that this boundary layer and wake behaviour has an impact on the accurate simulation of tonal noise, since the early transition to a 3D wake caused the simulation to produce acoustic results similar to a higher AOA. At a higher AOA the airfoil self noise mechanism switches to the TBL-TE, which is only capable of producing broadband noise. In Section 5.2.1, the experimental voltage signal for the 3° exhibited behaviour closest to the simulated acoustic signals for Case 4 and 4a. This also aligns with the C_p comparison at the beginning of this chapter, where the 1° simulated results were located between the 1° and 3° data sets. The narrowband spectra and the 1/3 octave band results for Case 4 and 4a are shown with the experimental 3° AOA data in Figure 5.20. The 3° experimental data appears to be a better match for the 1° AOA simulations,

meaning that the flow behaviour for these cases is that of a higher AOA. Since the 0° cases showed that the $3.4kHz$ tone is from the 2D to 3D boundary layer and wake transition, and the 1° cases were simulating an AOA closer to 3°, there must be some instability in the simulation that is initiating an early transition to 3D behaviour. It should also be noted that there is a potential that the closed test section used for the experiments could alter pressure and velocity in the flow and cause a delay in the transition to the 3D turbulent boundary layer behaviour.

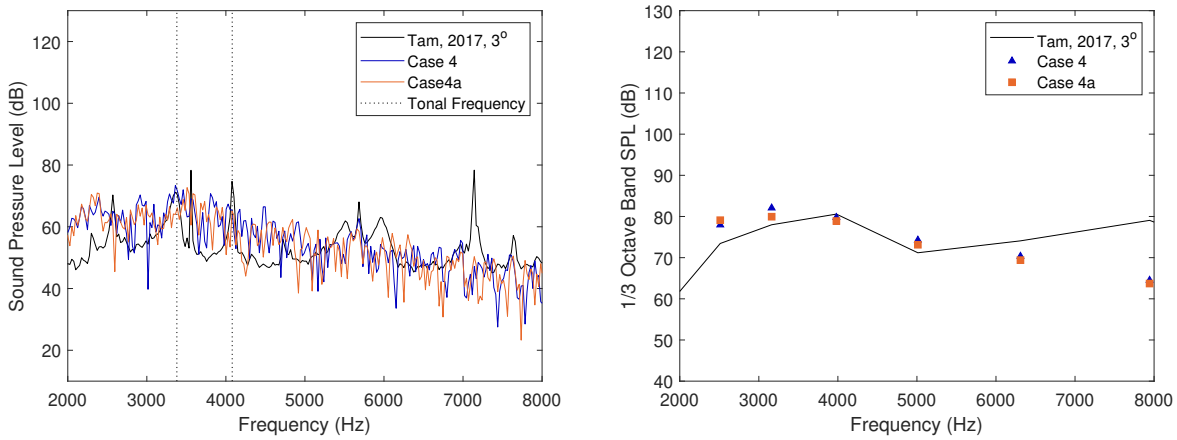

(a) Acoustic Spectra

(b) 1/3 Octave Band

Figure 5.20: Case 4 and 4a acoustic comparison with experimental 3° AOA data from Tam [35]

5.2.3 Static Pressure Results

The final set of acoustic results is the instantaneous pressure fluctuations in the free stream region of the flow field. These results are only present for the compressible cases, since these pressure changes are a result of compression of the air. This behaviour is present because the mesh spacing in the simulations is such that pressure-density waves can propagate through the solution at the speed of sound. This is the simulation method for a direct CAA simulation, and the SD 7037 cases meet the direct method simulation requirements because the small geometry allows for the correct node spacing relative to the speed of sound. These results are solely produced by the LES simulation, and are separate from the application of FW-H. The pressure fluctuation fields are shown in Figure 5.21 for Case

3 and 4 when the wake is both 2D and 3D. These images are taken from the same 2D and 3D results used in Section 5.1.3. All cases show that the sound produced is a dipole, with the waves radiating in the same pattern as shown in Figure 2.8. Though it is difficult to see in the images, the centre of the dipole pattern is located at the TE of the airfoil, which is the location specified by the LBL-VS and TBL-TE airfoil self-noise mechanisms. Dipoles are created from fluctuating force fields in the medium, and since there is a large fluctuating behaviour at the TE of the airfoil, it makes sense that the acoustic pressure would propagate in a dipole pattern.

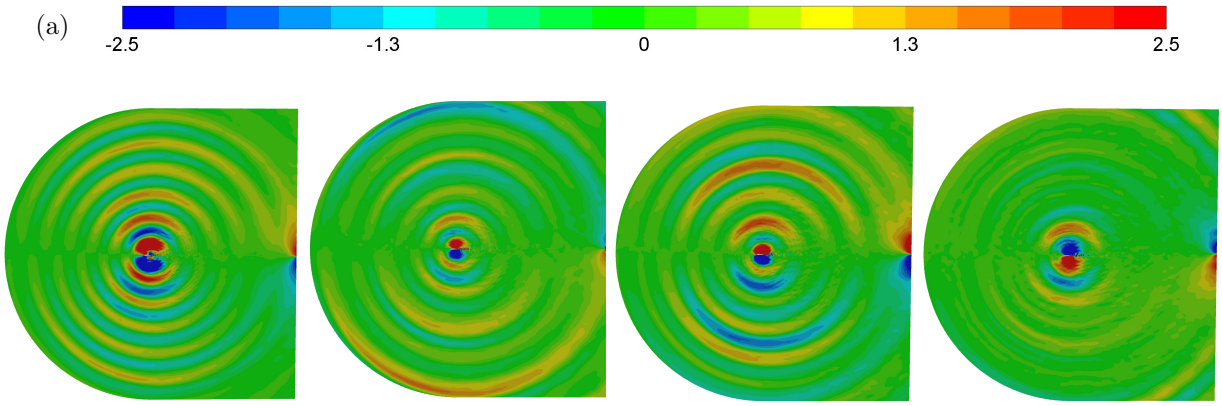

(b) Case 3 - 2D (c) Case 3 - 3D (d) Case 4 - 2D (e) Case 4 - 3D

Figure 5.21: Case 3 and 4 pressure fluctuations $(p - \bar{p})$ limited to narrow range

These pressure fluctuations reiterate the difference between the 2D and 3D behaviour near the TE and in the wake of the airfoil. The 2D results for both Case 3 and Case 4 show the strongest dipole pattern, and the 3D cases show weaker pressure waves. Figure 5.21e shows the weakest pattern because the 3D behaviour of Case 4 remains in that behaviour for long periods of time and therefore there is no strong tonal behaviour. In Case 3, the 3D behaviour is only present for a short time compared to the 2D behaviour and can maintain a dipole pattern throughout the entire simulation.

The other information gathered from these pressure fluctuations are the frequencies of the dominant tonal sources that cause the distinct pressure waves. These frequencies are determined from the wavelengths found in the plots of Figure 5.22. These are the instantaneous pressure fluctuations extracted for a plane extending from the TE of the airfoil to the top of the domain. For Case 3, the 2D results in Figure 5.22a have the most consistent pattern and the frequencies for each peak-to-peak wavelength range from 3.82 to $4.03kHz$, which is consistent with the proposal that the 2D behaviour is the cause of the

$4.1kHz$ tone. The 3D plot for Case 3 has frequencies ranging from 2.83 to $3.94kHz$ which averages to be the $3.4kHz$ tone, and since the 3D wake data is from the transition from 3D to 2D (see Figure 5.7a) it would make sense that the lower frequency tone is present. The Case 4 results range from 3.29 to $3.68kHz$ for the 2D behaviour and from 2.48 to $4.48kHz$ for the 3D behaviour. The 2D behaviour in this case is more irregular than the 2D behaviour for Case 3 because the consistent pattern is not present for long enough to develop the strong dipole fluctuations. It also has fluctuations much closer in frequency to the $3.4kHz$ tone since this is the dominant tone present at 1° AOA. The 3D behaviour has very irregular pressure fluctuations and a much lower amplitude than the other results, but the dominant frequencies are still within the range of the two tones. This can be seen in the narrowband acoustic spectra (Figure 5.18a) where the dominant highest SPL is in the 2 to $4.5kHz$ range.

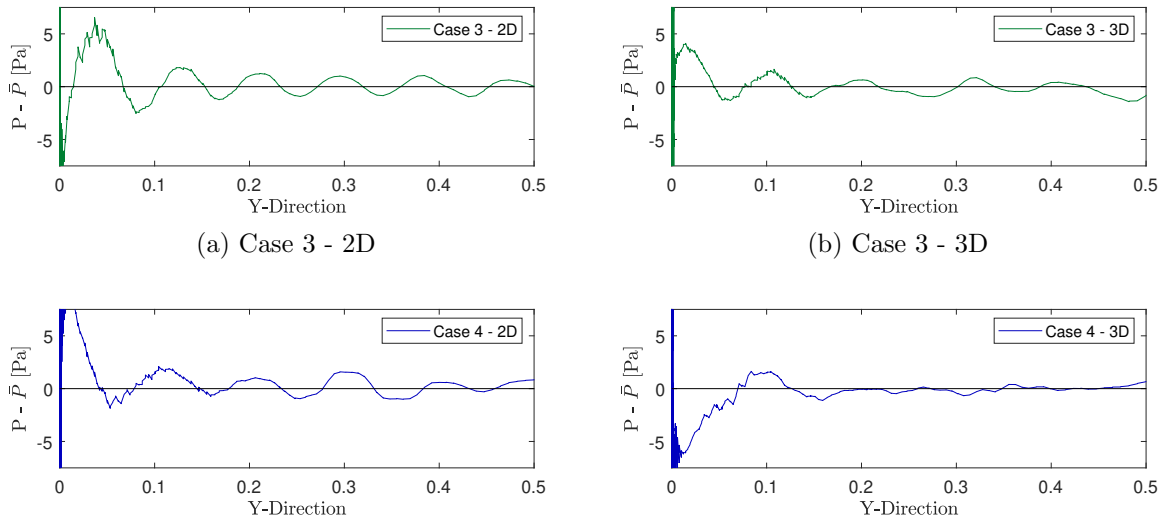

(a) Case 3 - 2D

(b) Case 3 - 3D

(c) Case 4 - 2D

(d) Case 4 - 3D

Figure 5.22: Case 3 and 4 pressure fluctuations ($p - \bar{p}$) for vertical plane above TE for both 2D and 3D behaviour

5.3 Discussion

Overall the SD 7037 simulation cases produce a good prectiction the flow behaviour and corresponding aeroacoustic noise for the given Re. Unknown sources of instability in the

compressible solution caused an alternating 2D and 3D wake behaviour that was reflected in the acoustic results. This instability may be caused by the density changes in the flow due to the density compression and expansion caused by the acoustic waves seen in Figure 5.21 or it may be caused by the setup of the simulation itself. Future work is planned to determine the cause of this instability, but for now, it reveals key information about the sources of the tonal noise produced by the LBL-VS self-noise mechanism. The incompressible Case 3a showed that the $4.1kHz$ tonal noise was generated when 2D behaviour in the wake passed the TE of the airfoil. The alternating 2D and 3D wake behaviour of the compressible Case 3 showed that the $3.4kHz$ tonal noise was generated in the transition between the 2D and 3D wake, and reiterated that the 2D boundary layer behaviour causes the $4.1kHz$ tone. This is shown clearly in Figure 5.17. These conclusions drawn from the 0° cases explained why the 1° cases produced an acoustic spectra similar to the 3° experimental results. To produce the experimentally measured 1° tone at $3.4kHz$, the boundary layer and wake behaviour would need to stay in a transitional state between the 2D and 3D behaviour, since this was shown to be the source of the tone at that frequency. For the majority of the 1° simulations, the boundary layer behaviour at the TE and in the wake was 3D, and therefore was not capable of predicting the tonal noise. The boundary layer behaviour for this Re and low AOAs is very sensitive to small changes, so further simulations are required to accurately simulate the flow and acoustics for the sharp tonal noise at 1° AOA.

Chapter 6

NACA 0012 Simulation Results and Discussion

This chapter contains the results of the NACA 0012 flow and aeroacoustic simulations performed and discusses predictive ability for the settings in Case 1 and Case 2. This simulation was originally intended as validation of the acoustic prediction method due to the large amount of experimental data available for the NACA 0012 airfoil. Interestingly, this case proved to be more complex due many reasons including its high Reynolds number of 1.5×10^6 and the large chord length of $30cm$. As a result, this simulation introduces a large amount of discussion on the setup requirements of CFD simulations when being used as the source information for the FW-H acoustic analogy.

6.1 Flow Results

The accuracy of the flow results greatly impacts the acoustic results since the acoustic model depends on the correct simulation of the boundary layer behaviour and the resulting surface pressure of the airfoil. When obtaining results from a LES simulation, these parameters are calculated at each time step to provide an instantaneous value, and averaged over the length of the simulation to produce mean values. Initial simulations for this research showed that simulating the mean values using LES was achievable, even if the mesh had insufficient resolution in the boundary layer. For this reason, the results presented in the following section are related to the instantaneous data collected, and its relation to, or fluctuation about, the mean values. All instantaneous data is from the same time step, which corresponds to the final data point in any time history plots.

6.1.1 Pressure, Lift and Drag Coefficients

The behaviour of a flow around an airfoil is most commonly represented through the lift, drag and pressure coefficient results. The instantaneous C_p results for Case 1 and 2 are shown in Figure 6.1, and are compared with the experimental data published by Gregory and O'Reilly [34]. By showing the instantaneous data, the transition point from a laminar boundary layer to a turbulent boundary layer can be seen at around $x/c = 0.3$ for both cases, when fluctuations about the mean C_p value become visible indicating spanwise variation. This transition will be discussed further in Section 6.1.3.

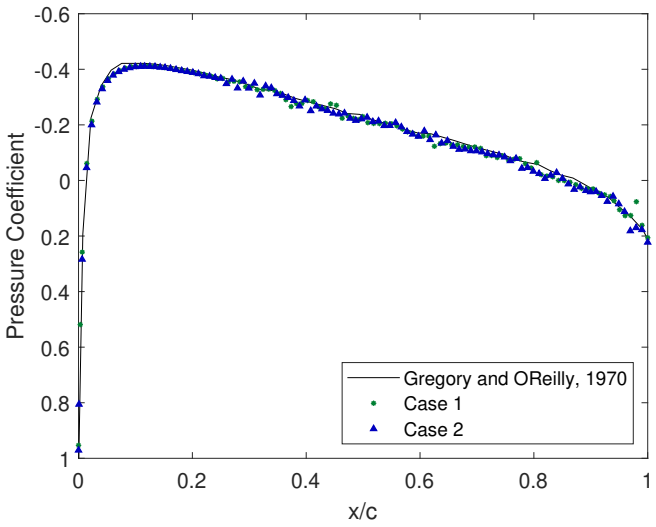

Figure 6.1: Case 1 and 2 instantaneous pressure coefficient compared with experimental data by Gregory and O'Reilly [34]

The symmetric NACA 0012 airfoil at 0° AOA is designed to have a lift coefficient of 0, and the simulated results shown in Figure 6.2a very closely predict the 0 mean value with fluctuations of $\pm 6 \times 10^{-3}$. The drag coefficient time histories, shown in Figure 6.2b, shows different repeating patterns, where Case 1 has disorganized fluctuations of small amplitude and Case 2 is largely a combination of a lower and higher frequency fluctuation. The experimental drag coefficient for $Re = 3 \times 10^6$ was measured as 0.0058 by Abbott and Von Doenhoff [33], and is higher than the simulated mean values. The drag coefficient behaviour is one of the key differences between Case 1 and 2, and has a strong correlation with the patterns present in the acoustic signals picked up by the receiver. The examination of the cause of this pattern will help to shed light on the requirements for an accurate acoustic

prediction.

(a)

(b)

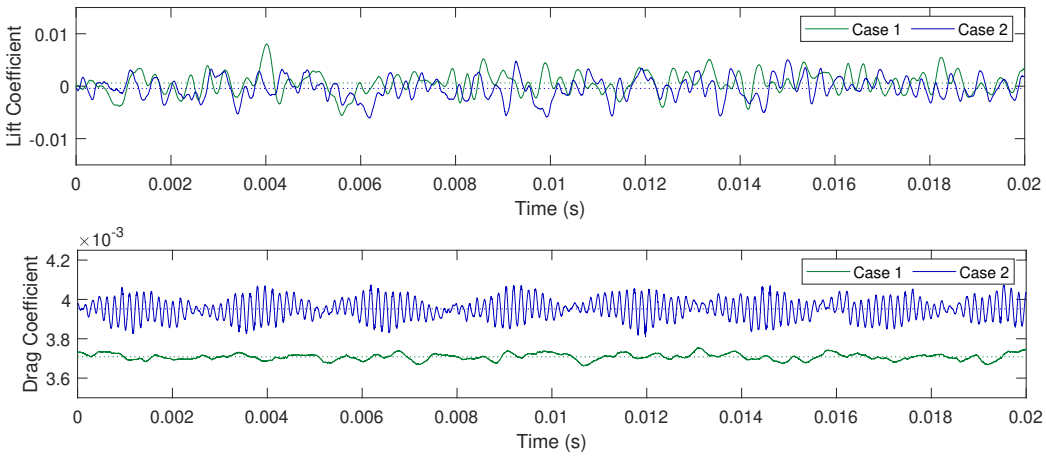

Figure 6.2: Case 1 and 2 lift and drag coefficient time histories for the final 20,000 time steps. Average values indicated by dotted line.

6.1.2 Velocity Field and Wake Behaviour

Figure 6.3b is a steady state velocity contour of the NACA 0012 airfoil at $Re = 10^6$, solved by Mittal *et al.* as a part of an incompressible RANS study of the airfoil [49]. The velocity field contours can be compared with the Case 1 and 2 instantaneous velocity magnitude contours in Figure 6.3c and 6.3d. The agreement is good for all three cases, and shows that the overall flow field is well simulated, with some minor differences in the wake close to the trailing edge. This area of the simulation is important to the acoustic prediction since the dominating airfoil self noise mechanism for this flow should be the TBL-TE mechanism, which radiates pressure waves from the trailing edge of the airfoil.

The behaviour in the wake changes based on the vortices that are shed from the trailing edge of the airfoil. This is visualized with the instantaneous Y-velocity magnitude to determine the differences between the behaviour in Case 1 and 2. Case 1, shown in Figure 6.4b, has larger fluctuations in the near wake region which causes wake fluctuations to occur further downstream of the airfoil. Figure 6.4c shows the wake for Case 2 has smaller pockets of positive and negative Y-velocity and has less disturbances occurring one chord length downstream. The cause of this difference in behaviour is investigated in the following section with analysis of the shear stress and skin friction behaviour on the surface of the airfoil.

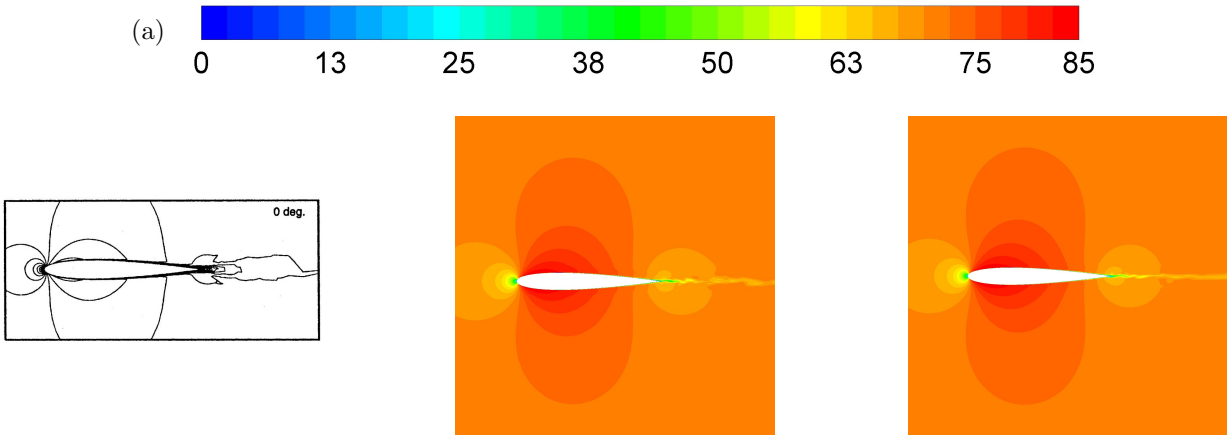

(b) Experimental (c) Case 1 (d) Case 2

Figure 6.3: Case 1 and 2 instantaneous velocity magnitude (m/s) compared with a steady-state solution of velocity magnitude at $Re = 10^6$ by Mittal *et al.* [49]

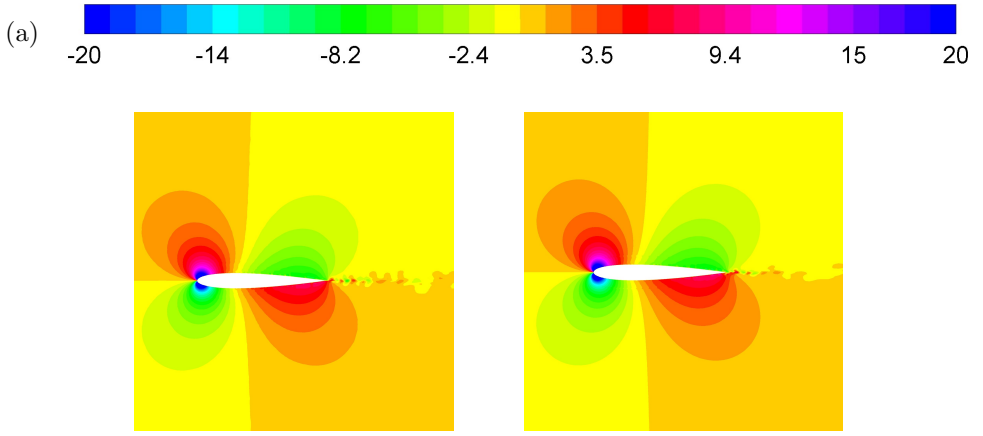

(b) Case 1 (c) Case 2

Figure 6.4: Case 1 and 2 instantaneous Y-velocity limited from -5 to $+5$ m/s

6.1.3 Surface Shear Stress

The final set of flow data for these NACA 0012 cases is an examination of the shear stress behaviour on the surface of the airfoil, since this is a strong indication of the boundary layer behaviour. These two cases have very thin boundary layers in the above images when compared with the SD 7037 results in the previous chapter, and this is due to the high Re for the NACA cases. Figure 6.5 shows the X-direction shear stress contour on the surface of the airfoil for both Case 1 and Case 2. As with the C_p plot for these cases, the instantaneous data for the shear stress shows clearly the location of boundary layer transition from laminar to turbulent behaviour. This occurs where the behaviour switches from being consistent in the spanwise direction to having spanwise variation, which indicates the transition to 3D boundary layer behaviour, as seen in Figure 2.3. For Case 1, this transition occurs further downstream and does not have as strong of a pattern develop immediately after transition. For Case 2, the transition causes large v-shaped ripples on the surface of the airfoil before developing randomized fluctuations downstream, which corresponds to region 3 in Figure 2.3.

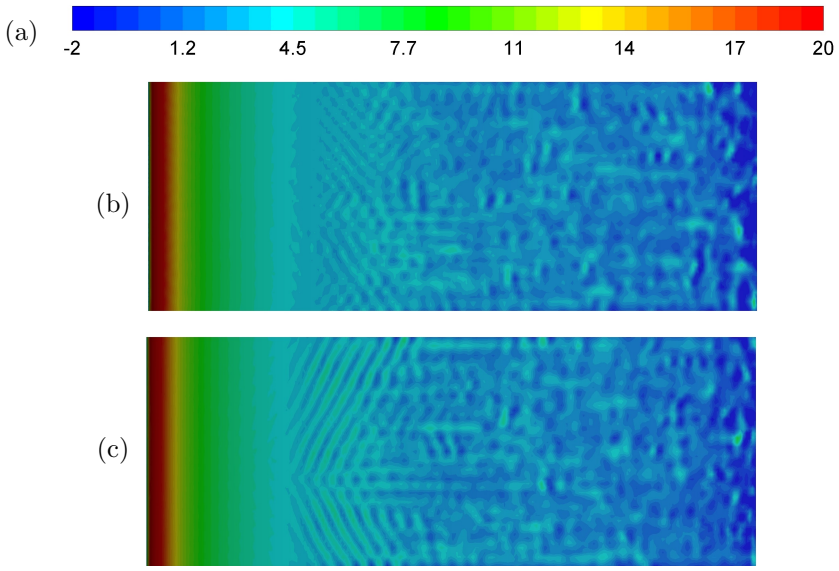

Figure 6.5: Instantaneous X shear stress contours from -2 to 20 Pa for (b) Case 1 and (c) Case 2

The difference in laminar to turbulent transition points is further emphasized on the skin friction coefficient plot in Figure 6.6. The turbulent behaviour begins when the skin

friction coefficient decreases and fluctuates due to the added turbulence in the boundary layer. For Case 1, the larger amplitude fluctuations begin at around $x/c = 0.3$, which is the same prediction from the C_p plot. Case 2, however, begins the transition at around $x/c = 0.25$, which could explain the differences in the trailing edge and wake behaviour noted above. The large dimensions of the airfoil means that the transition for Case 2 is occuring $1.5cm$ upstream from the Case 1 location, giving the turbulent boundary layer more time to develop. The added turbulence in the boundary layer would explain the irregular and weaker pattern in the Y-velocity contours for Case 2.

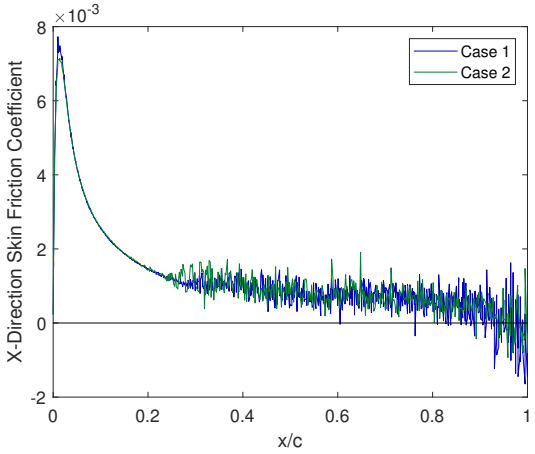

(a) Skin Friction Coefficient

Case	C_d	Mean C_f
1	0.00371	0.00126
2	0.00395	0.00130
Exp. [33]	0.0058	–

(b) Contribution to Drag

Figure 6.6: Case 1 and 2 skin friction coefficient vs x/c calculated using x-direction shear. Summary of average drag coefficient and average skin friction coefficient compared with experimental drag coefficient by Abbott and Von Doenhoff [33]

The average of the skin friction coefficients for Case 1 and 2 are listed in Figure 6.6b to represent the contribution of skin friction drag to the overall drag coefficient. The difference between the mean skin friction coefficient values is not significant when compared to the difference in the overall drag coefficients, which indicates that the differences in the drag comes from higher pressure drag for Case 2. It should also be noted that the difference in the average drag coefficients is 2.4×10^{-4} and is not significant when compared to the experimental drag value which is 2×10^{-3} larger than the simulated values [33]. This does not provide an explanation for the regular patterns in the Case 2 drag coefficient, since a more turbulent boundary layer would be expected to have irregular behaviour with respect to time. The mesh for Case 2 is much finer and could either be more accurately simulating the transient behaviour of the flow, or it could be introducing error into the solution due

to the areas with higher skew and lower quality. The simulations for both Case 1 and 2 are also incompressible, and there may be errors due to compressibility since the Mach number for the NACA cases is 0.21.

6.2 Acoustic Results

The application of the FW-H acoustic analogy to the LES data for Case 1 and Case 2 determines the acoustic pressure fluctuations in the flow at the location of the receiver. Though the simulated flow shows few differences, the acoustic pressure measurements shown in Figure 6.7 differ greatly. The Case 1 receiver has a much lower acoustic pressure amplitude and has a much less consistent structure when compared to the high amplitude fluctuations for Case 2. The differences between the cases resemble the patterns found in the drag time history in Figure 6.2b, strongly suggesting a link between the flow properties responsible for both effects.

(a)

(b)

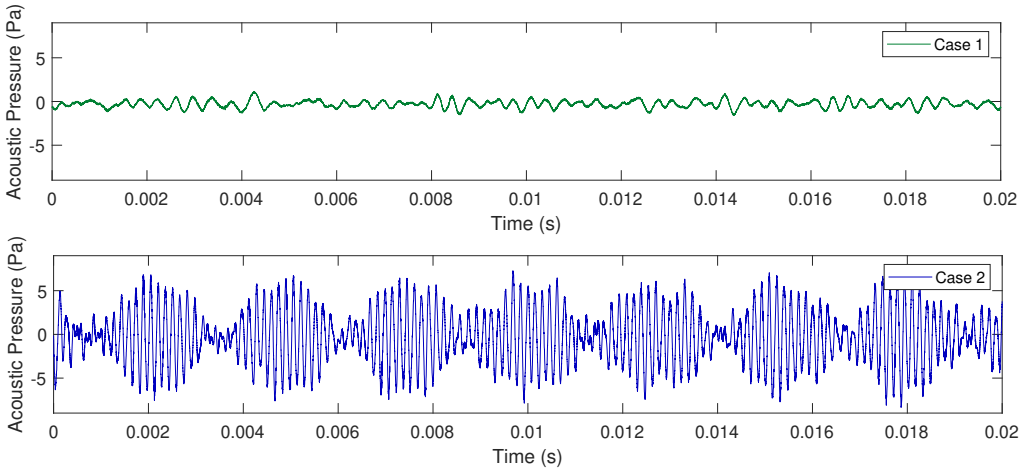

Figure 6.7: Case 1 and 2 acoustic pressure signal (Pa) at the receiver for the final 20,000 time steps

The acoustic results were processed using the FFT function in MATLAB. The acoustic pressure files were altered to remove the data gathered before the solution reached a statistically steady state. This was judged by the behaviour in the lift and drag time histories and in the acoustic pressure file itself. Case 2 had a total run time of $0.0345s$ and became statistically steady after $0.0075s$, leaving $0.027s$ of acoustic data for processing. Case 1 had a total run time of $0.1s$ and became statistically steady at approximately $0.01s$, leaving

$0.09s$ of acoustic data for processing. To make a fair comparison of the acoustic pressure amplitudes between the two cases, the bin sizes for the FFT were kept constant. This is achieved by keeping the signal length constant, therefore only the last $0.027s$ of the Case 1 acoustic data was processed.

The narrowband SPL comparison in Figure 6.8a shows that the broadband components of the noise for both cases follow the same general trend. The difference is the tonal noise components found in Case 2 around $6kHz$ and $11kHz$. This is further emphasized in the 1/3 octave band data in Figure 6.8b, where the two tones can be clearly seen in the high frequency range of the results. Both cases overpredict the SPL of the NACA airfoil, but generally follow the overall trend of the experimental data. The data by Brooks *et al.* has very similar SPL patterns for the tripped and untripped boundary layer experiments, but the tripped case has a higher SPL for the lower frequencies and is closer to the SPL of the simulated cases. This brings up the potential that the simulation has been numerically tripped due to the coarseness of the mesh for the given dimensions. This would shift the transition to turbulence further upstream than in the untripped experimental flow, and would affect the boundary layer interaction at the TE which in turn affects the acoustic behaviour.

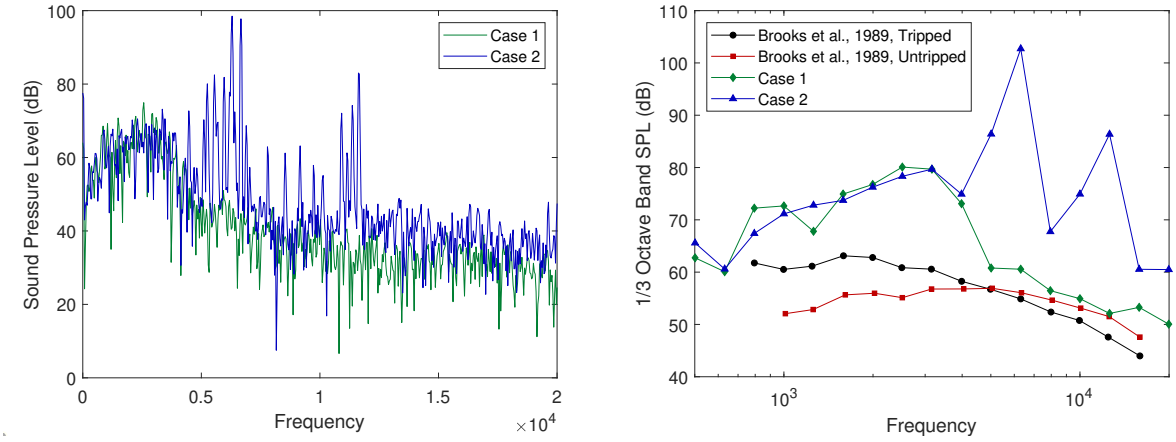

(a) Acoustic Spectra

(b) 1/3 Octave Band

Figure 6.8: Case 1 and 2 narrowband and 1/3 octave band SPL results compared with tripped and untripped experimental results by Brooks *et al.* [6]

The NACA 0012 airfoil has produced tones at lower Reynolds numbers, and the experimental data shows that the tonal noise mechanism disappears around $Re = 7.2 \times 10^5$ [6].

Since the LBL-VS self-noise mechanism is known to produce tonal noise, and the TBL-TE mechanism creates broadband noise, it is possible that even though Case 2 has been shown to simulate a turbulent boundary layer, the simulation must be producing patterns that replicate the LBL-VS self noise mechanism. This calls into question the stability of the Case 2 solution, which will require further investigation since the cause of this pattern in the drag coefficient and acoustic results is not apparent given the current analysis.

6.3 Discussion

The NACA 0012 simulation cases bring up an interesting issue in the acoustic simulation: the false generation of tonal noise. In the SD 7037 cases, there was difficulty simulating the high SPL tonal noise for the 1° AOA flow. This means that depending on the geometry of the simulation, there can either be a concern with the false generation of tones, or the inability to simulate tones. The NACA cases feature a high Re and physically large geometry, which required a fine mesh to get an accurate simulation of the transient fluctuations of properties on the airfoil surface (especially near the TE). The SD cases were for a low Re and physically small geometry, and could easily achieve a fine mesh that essentially meets the criteria for a direct computation of acoustic pressure waves. The SD airfoil did have a more complex boundary layer to simulate due to the presence of a LSB and the sensitive feedback mechanisms required for its creation. All simulations obtained flow results that matched experimental data for the given Re, and produced a good prediction of the broadband components of the noise and had varying success with the tonal noise components.

Both simulation geometries resulted in a similar transient pattern in the lift coefficient, drag coefficient and acoustic signal histories. Specifically, the compressible cases for the SD 7037 geometry (Case 3 and 4) and the fine mesh simulation of the NACA 0012 geometry (Case 2). Further investigation is required into the cause of this pattern, but it is hypothesized that the pattern is either due to similar patterns occuring in the experimental flows or instabilities in the simulation. Due to time limitations of this research and the long run times for the simulations, a formal grid independence study and sensitivity analysis was not conducted, though the meshes for both geometries were gradually made finer to improve the acoustic prediction. These studies would clarify the source of the inaccuracies of the noise prediction by determining the cause of missing tonal noise or the generation of false tones.

Chapter 7

Conclusions and Recommendations

This research tested the ability of computational aeroacoustic methods to predict the airfoil self-noise generated by the SD 7037 and NACA 0012 airfoils at static AOAs. The simulations used RANS to initialize the flow and LES and the FW-H analogy for simulation of the transient flow field and acoustics, respectively. The SD 7037 cases were performed for 0° and 1° AOAs and compared with the low Re experimental flow data from Ghorbanishohrat and acoustic measurements by Tam [2] [35]. Each AOA was simulated using incompressible LES and compressible LES, which resulted in an accurate prediction of the flow behaviour, especially considering the complexities of the LSB generated for this low Re flow. The 0° results showed that the $4.1kHz$ tonal noise was a result of the 2D boundary layer behaviour at the TE of the airfoil, and that the $3.4kHz$ tone was a result of the transition between 2D and 3D boundary layer behaviour. The combination of these behaviours resulted in an accurate prediction of the narrowband and 1/3 octave band acoustic spectra for the SD 7037 airfoil at 0°. The 1° results should have predicted the sharp $3.4kHz$ tonal noise found in the experiments, but the flow simulation resembled the boundary layer and acoustic behaviour closer to 2° or 3° AOA. This could be seen with the transition to 3D boundary layer behaviour, which should occur at a higher AOA according to the experimental data. The NACA cases produced an accurate simulation of the flow behaviour at the given Re, but resulted in an over-prediction of the SPL when compared to the experimental data by Brooks *et al.* [6]. These simulations used incompressible LES and though the flow results were similar between the two cases, Case 2 predicted tonal noise that was not present in the experimental data.

Overall the predictive ability of the LES and FW-H acoustic analogy matches well with experimental flow and acoustic data. Care must be taken when setting up the simulation, since the requirements for the mesh and solution settings are strict. Errors caused by

instabilities in the simulation led to missing tonal noise prediction for the SD 7037 1° cases and also led to the creation of false tonal noise in one of the NACA 0012 cases. Due to the long compute times required for these simulations and the limited time frame for this research, the source of these instabilities to cause a lack of tonal noise prediction or false tonal noise was not determined. Recommendations for future work are to perform a grid independence study along with an analysis to determine the conditions that cause the instabilities. Future steps required for the application of the LES and FW-H analogy to wind turbine aeroacoustic prediction is to test the model for oscillating AOAs and then application of the model to a rotating blade segment. The results of this research indicates that the power of the aeroacoustic prediction model has the potential to be applied to the prediction of wind turbine noise.

References

[1] H. Schlichting and K. Gersten, *Boundary-Layer Theory*. Springer-Verlag Berlin Heidelberg, 9th ed., 2017.

[2] F. Ghorbanishohrat, *Study of a low Re airfoil considering laminar separation bubbles in static and pitching motion*. PhD thesis, University of Waterloo, 2019.

[3] F. M. White, *Fluid Mechanics*. New York: McGraw Hill, 8th ed., 2016.

[4] G. Leventhall, "Basic Acoustics," in *Wind Turbine Noise*, ch. 1, pp. 1–11, Essex: Multi-Science Publishing Co. Ltd., 2011.

[5] S. Wagner, R. Bareiss, and G. Guidata, *Wind Turbine Noise*. Berlin: Springer-Verlag Berlin Heidelberg, 1996.

[6] T. F. Brooks, S. Pope, and M. A. Marcolini, "Airfoil Self-Noise and Prediction," tech. rep., NASA Reference Publication 1218, 1989.

[7] R. Paterson, P. G. Vogt, M. R. Fink, and C. Munch, "Vortex Noise of Isolated Airfoils," *Journal of Aircraft*, vol. 10, no. 5, pp. 293–302, 1973.

[8] C. K. W. Tam, "Discrete Tones of Isolated Airfoils," *Journal of Acoustical Society of America*, vol. 55, no. 6, pp. 1173–1177, 1974.

[9] M. R. Fink, "Prediction of Airfoil Tone Frequencies," *Journal of Aircraft*, vol. 12, no. 2, pp. 118–120, 1975.

[10] S. E. Wright, "The acoustic spectrum of axial flow machines," *Journal of Sound and Vibration*, vol. 45, no. 2, pp. 165–223, 1976.

[11] H. Arbey and J. Bataille, "Noise generated by airfoil profiles placed in a uniform laminar flow," *Journal of Fluid Mechanics*, vol. 134, pp. 33–47, 1983.

[12] S. Oerlemans, "Primary Noise Sources," in *Wind Turbine Noise*, ch. 2, pp. 13–45, Essex: Multi-Science Publishing Co. Ltd., 2011.

[13] P. Totaro, "Noise Reduction Technologies, Current and Futrue," in *EWEA 2014*, (Barcelona), 2014.

[14] Global Wind Energy Council, "Global Wind Energy Report: Annual Market Update 2017," tech. rep., Brussels, 2017.

[15] S. Oerlemans, P. Sijtsma, and B. Méndez López, "Location and quantification of noise sources on a wind turbine," *Journal of Sound and Vibration*, vol. 299, no. 4-5, pp. 869–883, 2007.

[16] S. Oerlemans, "Wind Tunnel Aerodynamic Tests of Six Airfoils for Use on Small Wind Turbines," Tech. Rep. 35339, NREL Subcontractor Report, 2004.

[17] A. E. Bale, *The Application of MEMS Microphone Arrays to Aeroacoustic Measurements*. PhD thesis, University of Waterloo, MASc Thesis, 2011.

[18] R. K. Amiet, "Acoustic radiation from an airfoil in a turbulent stream," *Journal of Sound and Vibration*, vol. 41, no. 4, pp. 407–420, 1975.

[19] P. Moriarty and P. Migliore, "Semi-empirical aeroacoustic noise prediction code for wind turbines," Tech. Rep. NREL/TP-00-34478, National Renewable Energy Labratory (NREL), Colorado, 2003.

[20] K. Boorsma and J. G. Schepers, "Enhanced wind turbine noise prediction tool SILANT," *Fourth International Meeting on Wind Turbine Noise, Rome, Italy*, no. FEBRUARY, pp. 12–14, 2011.

[21] P. Moriarty, "NAFNoise User's Guide," tech. rep., National Renewable Energy Laboratory, 2005.

[22] P. Moriarty, G. Guidata, and P. Migliore, "Prediction of Turbulent Infow and Trailing-Edge Noise for Wind Turbine," in *11th AIAA/CEAS Aeroacoustics Conference*, 2005.

[23] P. Moriarty, G. Guidata, and P. Migliore, "Recent Improvement of a Semi-Empirical Aeroacoustic Prediction Code for Wind Turbines.pdf," in *10th AIAA/CEAS Aeroacoustics Conference*, 2004.

[24] H. Youngren and M. Drela, "XFOIL 6.9 User Guide," tech. rep., Massachusetts Institute of Technology (MIT), 2001.

[25] M. V. Lowson, "Assessment and Prediction of Wind Turbine Noise," tech. rep., Energy Technology Support Unit (ETSU) Department of Trade and Industry, Flow Solutions Ltd., 1993.

[26] ANSYS Academic Research, "ANSYS Fluent Theory Guide, Release 18," in *ANSYS Help System*, SAS IP Inc., 2018.

[27] C. K. W. Tam, "Computational Aeroacoustics : An Overview of Computational Challenges and Applications," vol. 18, no. August, pp. 547–567, 2004.

[28] D. G. Crighton, "Computational Aeroacoustics for Low Mach Number Flows," in *Computational Aeroacoustics*, ch. Classical, pp. 50–68, New York: Springer-Verlag New York, 1993.

[29] F. Farassat, "The Acoustic Analogy as a Tool of Computational Aeroacoustics," in *Computational Aeroacoustics*, ch. Mathematic, pp. 133–155, New York: Springer-Verlag New York, 1993.

[30] M. Lighthill, "On Sound Generated Aerodynamically . I . General Theory," *Proceedings of the Royal Society of London, Series A, Mathematical and Physical Sciences*, vol. 211, no. 1107, pp. 564–587, 1952.

[31] J. Ffowcs Williams and D. Hawkings, "Sound Generation by Turbulence and Surfaces in Arbitrary Motion," *Philisophical Transactions of the Royal Society of London. Series A, Mathematical and Physical Sciences*, vol. 264, no. 1151, pp. 321–342, 1969.

[32] F. Farassat, "Derivation of Formulations 1 and 1A of Farassat," *Nasa/TM-2007-214853*, vol. 214853, no. March, pp. 1–25, 2007.

[33] I. H. Abbott and A. E. Von Doenhoff, *Theory of Wing Sections, Including a Summary of Airfoil Data*. Mineola, NY: Dover Publications, 1959.

[34] N. Gregory and C. O'Reilly, "Low-Speed Aerodynamic Characteristics of NACA 0012 Aerofoil Section," *Ministry of Defence Aeronautical Research Council*, vol. 3726, 1970.

[35] N. Tam, "An Aeroacoustic Study of Airfoil Self-Noise for Wind Turbine Applications," Master's thesis, University of Waterloo, 2017.

[36] W. R. Wolf, J. L. F. Azevedo, and S. K. Lele, "Convective effects and the role of quadrupole sources for aerofoil aeroacoustics," *Journal of Fluid Mechanics*, vol. 708, pp. 502–538, 2012.

[37] S. H. Wasala, *Numerical Analysis and Aeroacoustic Simulation of Noise from Wind Turbines*. Phd thesis, University of Auckland, PhD Thesis, 2016.

[38] *ANSYS Fluent, Release 18*. SAS IP Inc., 2016.

[39] *MATLAB, Version R2018b*. The Mathworks Inc., 2018.

[40] H. K. Versteeg and W. Malalasekera, *An Introduction to Computational Fluid Dynamics, The Finite Volume Method*. Harlow: Pearson Education Limited, 2nd ed., 2007.

[41] K. S. Brentner and F. Farassat, "An Analytical Comparison of the Acoustic Analogy and Kirchoff Formulation for Moving Surfaces," in *American Helicopter Society 53rd Annual forum*, (Virginia Beach), NASA, 1997.

[42] Brentner, "An Efficient and Robust Method for Predicting Helicopter High-Speed Impulsive Noise," *Journal of Sound and Vibration*, vol. 203, no. 1, pp. 87–100, 1997.

[43] M. Casey and T. Wintergertse, "Quality and Trust in Industrial CFD" Best Practice Guidelines," tech. rep., European Research Community on Flow, Turbulence and Combustion (ERCOFTAC), 2000.

[44] SHARCNET, "SHARCNET, Ontario's network of high-performance computer clusters," 2018.

[45] ComputeCanada, "Compute Canada, Advanced computing services in support of research," 2018.

[46] M. S. Selig, C. A. Lyon, P. Giguere, C. P. Ninham, and J. Guglielmo, *Summary of low-speed airfoil data, Vol. 2*. VA: SoarTech Publications, 1996.

[47] K. Gharali, *Pitching airfoil study and freestream effects for wind turbine applications*. PhD thesis, University of Waterloo, 2013.

[48] F. Ghorbanishohrat and D. A. Johnson, "Oil Flow Visualization of the Laminar Separation Bubble on a SD 7037 Airfoil," in *25th Canadian Congress of Applied Mechanics (CANCAM)*, (London, Ontario, Canada), pp. 257–260, 2015.

[49] S. Mittal and P. Saxena, "Hysteresis in flow past a NACA 0012 airfoil," *Computer Methods in Applied Mechanics and Engineering*, vol. 191, pp. 2179–2189, 2002.

APPENDICES

Appendix A

Matlab Code for Acoustic Processing

```
%Acoustic File Parameters
timestep=0.000001;
omit_ts=42500;
num_ts=81000;
num_rows=num_ts-33;

%Extract and Calculate SPL for each receiver
for rec=1:1:15
    rec_file = sprintf('receiver-%d.ard',rec);
    new_signal = dlmread(rec_file," ",[4 0 num_rows 1]);
    %Remove specified number of time steps from start of signal
    Start_time=new_signal(1,1)+timestep*omit_ts;
    new_signal=new_signal(omit_ts:end,:);
    %set simulation time
    time=new_signal(:,1);
    signal_length=length(time);
    sample_freq=1/timestep;
    %extract pressure data from time data
    Pressure_1=new_signal(:,2);
    %bandpass filter
    Pressure_x=highpass(Pressure_1,1000,sample_freq);
    Pressure_2=lowpass(Pressure_x,10000,sample_freq,'steepness',0.95);
    %window signal
    window=hamming(signal_length);
```

```
    Pressure=window.*Pressure_2;
    %perform FFT
    Acoustic_Spectrum=fft(Pressure,signal_length);
    %frequency domain
    frequency=sample_freq*(0:(signal_length/2))/signal_length;
    %two sided spectrum then 1 sided spectrum
    P2=abs(Acoustic_Spectrum/signal_length);
    P1=P2(1:floor(signal_length/2)+1);
    P1(2:end-1)=2*P1(2:end-1);
    %Change from pressure to SPL
    Ref_P=2E-5;
    P1_abs=P1(:)+Ref_P;
    SPL(:,rec)=10*log10(P1_abs.^2/Ref_P^2);
end
%sum SPL data from all receivers
power_SPL = 10.^(SPL./10);
added_SPL = sum(power_SPL,2);
%Narrowband spectra results
new_SPL = 10*log10(added_SPL);
%1/3 octave band edges
data=10.^(0.1.*[1:50]);
band_edges=data(1,:)./10^0.05;
band_num=discretize(frequency,band_edges);
%add 1/3 octave bands
data(2,:)=zeros;
power = 10.^(new_SPL./10);
[j,k]=size(SPL);
for i=1:1:j
    band=band_num(i);
    test=isnan(band);
    if isnan(band)==0
        data(2,band)=power(i)+data(2,band);
    end
end
%1/3 octave results
data(2,:)=10*log10(data(2,:));
```